Contents lists available at ScienceDirect

Composite Structures

Passively morphing trailing edge design for composite tidal turbine blades

James M. Maguire [a,*], Dimitrios Mamalis [a,b], Shūji Ōtomo [c,d], Edward D. McCarthy [a]

[a] School of Engineering, Institute for Materials and Processes, The University of Edinburgh, Edinburgh EH9 3FB, UK
[b] Offshore Renewable Energy Catapult, Blyth, NE24 1LZ, UK
[c] School of Engineering, Institute for Energy Systems, The University of Edinburgh, Edinburgh EH9 3FB, UK
[d] Graduate School of Engineering, Tokyo University of Agriculture and Technology, Koganei, Tokyo, 184-8588, Japan

ARTICLE INFO

ABSTRACT

Numerical simulations and lab-scale experiments are used to evaluate three passively morphing trailing edge designs for a composite tidal turbine blade. The designs include a closed trailing edge, an open trailing edge, and a corrugated trailing edge. It is shown that geometric stiffness, as well as material stiffness, play key roles in achieving the desired deformation of the trailing edge. One trailing edge design is down-selected for further investigation via full-scale numerical simulations. These simulations demonstrate how the composite lay-up influences the morphing response of the trailing edge and its likelihood of material failure. The influence of camber is also investigated in terms of both material behaviour and hydrodynamic performance. Finally, the potential for bend-twist coupling of the laminate skins is explored.

1. Introduction

Tidal energy is well documented for its potential as a predictable renewable energy resource in coastal regions [1]. In recent years, this potential has begun to be realised as industry transitions towards commercialisation, with several full-scale devices deployed around the world [2,3]. With tidal energy development being several decades behind that of wind energy and solar energy, there is a pressing need to reduce costs and improve reliability to make it more competitive [1,3]. One means of achieving this is by mitigating excess load fluctuations applied to the turbine, which can be severe and have caused the failure of several blades and generators [3].

To reduce excess loads, the blades can be pitched to alter their angle of attack [4]. While active and passive pitching mechanisms exist for tidal turbine blades, the former cannot react fast enough to mitigate unsteady load fluctuations due to wave interaction, wake interaction, vortex shedding, etc. [5]. Bend-twist coupling is a passive pitching mechanism that has seen considerable development; it has been deployed in towing tank and flume testing of prototype turbines [6–10]. In this instance, the composite lay-up of the blade is designed to induce span-wise twisting as the blade bends. As such, the angle of attack changes more towards the tip of the blade, with reductions in thrust load, up to 11 %, recorded in towing tank tests [9].

In contrast to bend-twist coupling, theoretically, a morphing blade

that changes its angle of attack uniformly along its span can achieve greater load mitigation [5]. Several such concepts make use of a flexible trailing edge (TE) to achieve this chordwise morphing strategy [11–14]. Typically, a high degree of material compliance is required to enable the necessary chordwise bending deformations, with the aforementioned concepts often making use of elastomeric materials for prototype blades. However, with the exception of one design [13], these tidal turbine blade concepts have seen a low level of development; technology readiness level (TRL) 1 – 3. In this regard, prototype blades have been over-reliant on design and manufacturing techniques that are not scalable for such structures (e.g. 3D printing) [12,15]. Moreover, little or no consideration is given to the durability of the associated materials, i.e., even in the event that load fluctuations are mitigated by pitching, the blades must continuously withstand enormous thrust loads (>250 kN) to generate power [16]. For passively morphing TE concepts to reach higher TRLs, it is necessary to consider how they may be realised with proven industrial materials and manufacturing methods, such as vacuum-assisted resin transfer moulding (VaRTM) of fibre-reinforced composites.

In this work, a selection of passively morphing TE designs is investigated for use in composite tidal turbine blades. Composite materials are widely used in tidal turbine blade production due to their corrosion resistance, high stiffness and strength, and high fatigue tolerance [4]. Moreover, the possibility to control fibre orientation means that their mechanical properties can be tailored to the structural requirements of

---

Nomenclature

BEMT	Blade element momentum theory
DIC	Digital image correlation
FEA	Finite element analysis
HATT	Horizontal axis tidal turbine
HDPU	High-density polyurethane
IPS	In-plane shear
LE	Leading edge
LT	Longitudinal tensile
PLA	Polylactic acid
QI	Quasi-isotropic
TE	Trailing edge
TRL	Technology readiness level
TT	Transverse tensile
UD-GF	Unidirectional glass fibre
U2	Displacement in y-direction [m]
VaRTM	Vacuum-assisted resin transfer moulding
VATT	Vertical axis tidal turbine
VIP	Vacuum infusion process
α	Angle of attack [°]
α_0	Initial angle of attack [°]
δ	Maximum deflection [m]
θ	Corrugation angle [radians or °]
ν	Poisson's ratio [-]
ν_{12}	In-plane Poisson's ratio [-]
ρ	Material density [kg/m^3]
ρ_∞	Water density [kg/m^3]
σ_{11}	Normal stress in the longitudinal direction [MPa]
σ_{22}	Normal stress in the transverse direction [MPa]
τ_{12}	In-plane shear stress [MPa]
φ	Composite volume [m^3]
A_C	Cross-sectional area of trailing edge skin [m^2]
A_{11}	Axial stiffness [N/m]
$\overline{A}_{11}$	Axial stiffness of trapezoidal corrugation [N/m]
b	Blade span [m]
C_D	Drag coefficient [-]
C_L	Lift coefficient [-]
C_P	Pressure coefficient [-]
c	Length of corrugated semi-period [m]
d	Distance from neutral axis to centre of mass of section [m]
D_{11}	Bending stiffness [N m]
$\overline{D}_{11}$	Bending stiffness of trapezoidal corrugation [N m]
E	Young's modulus [MPa]
E_{11}	Young's modulus in morphing direction [MPa]
E_1^C	Longitudinal compressive modulus [GPa]
E_1^T	Longitudinal tensile modulus [GPa]
E_2^C	Transverse compressive modulus [GPa]
E_2^T	Transverse tensile modulus [MPa or GPa]
F_B	Buoyancy force [N]
F_D	Drag force [N]
F_G	Gravity force [N]
F_L	Lift force [N]
F_T	Thrust force [N]
F_O	Rated lift force [N]
F_1, F_2	Tsai-Wu fitting parameters [MPa^{-1}]
F_{11}, F_{22}	Tsai-Wu fitting parameters [MPa^{-2}]
F_{66}	Tsai-Wu fitting parameter [MPa^{-2}]
F_{12}	Biaxial strength interaction parameter [MPa^{-2}]
F_{12}^*	Biaxial strength interaction coefficient [-]
G_{12}	In-plane shear modulus [GPa]
f	Load frequency [Hz]
g	Acceleration due to gravity [m^2/s]
h	Height of the semi-period corrugation [m]
I	Second moment of area [m^4]
I_C	Second moment of area of closed trailing edge [m^4]
I_O	Second moment of area of open trailing edge skin [m^4]
I_1, I_2	Geometric parameters for corrugation [m]
k	Reduced frequency [-]
L	Chord length [m]
l	Length of trailing edge [m]
P	Pressure [Pa]
P_∞	Freestream pressure [Pa]
q	Distributed load [N/m]
r	Base length of corrugation [m]
S	In-plane shear strength [MPa]
s	Length of corrugated profile [m]
t	Skin thickness [m]
V_O	Rated water velocity [m/s]
V_R	Relative water velocity [m/s]
V_∞	Freestream water velocity [m/s]
X_C	Longitudinal compressive strength [MPa]
X_T	Longitudinal tensile strength [MPa]
x	Coordinate along chord line [m]
Y_C	Transverse compressive strength [MPa]
Y_T	Transverse tensile strength [MPa]

the blade, while maintaining slender hydrofoil profiles [7,17]. Initial evaluation of the designs and their morphing function is performed using a quasi-steady finite element analysis. Prototype blades are manufactured from a flexible composite material system and are tested in a water flume to compare with the numerical models. From the results, one TE design is down-selected for scaled-up simulations, in which a variety of composite design concepts are explored for tailoring the stiffness of the TE. While the scaled-up simulations do not constitute actual design cases, they offer valuable insight into how a flexible TE may be designed and implemented at full-scale

2. Methodology

In this section, the basis for three flexible TE designs is presented. Details are given for the numerical and experimental analyses used to test the three designs at lab-scale. Additionally, the full-scale simulation methodology is described.

2.1. Blade design

There are a wide variety of tidal turbine designs currently in existence [1], but two main categories will be considered herein: horizontal axis tidal turbines (HATT) and vertical axis tidal turbines (VATT); basic examples of which can be seen in Fig. 1(a) and (b), respectively. In each case, the cross-section of the blade is defined by a hydrofoil geometry, as shown in Fig. 1(c). For HATTs, the hydrofoil will typically vary along the span of the blade to account for changes in relative water velocity. Variations to the hydrofoil may include chord length, pitching angle, hydrofoil profile, and composite laminate lay-up [17]. For VATTs, it is common for the hydrofoil to remain constant along its span [13,18,19], however, there are cases where the blade is twisted helically about the central axis of rotation [20].

To simplify the analysis of the passively morphing TEs in this study, each blade is designed with constant hydrofoil geometry and dimensions along its span, similar to a VATT blade (i.e., it is a constant-section extrusion of one blade profile). While this may not be representative
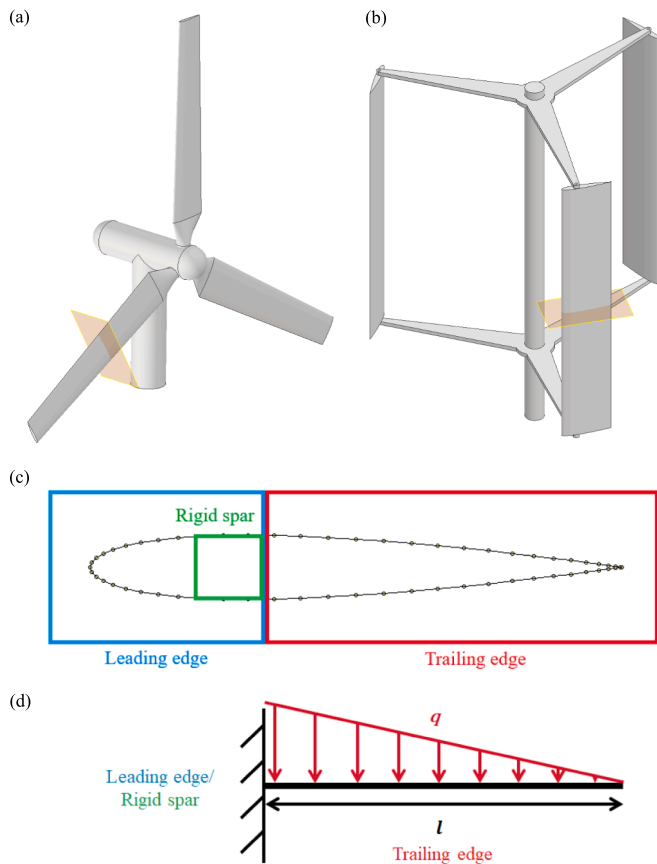
Fig. 1. A typical (a) horizontal axis tidal turbine (HATT) and (b) vertical axis tidal turbine (VATT). (c) The NACA 0012 geometry used in this study with its leading edge (LE), trailing edge (TE), and spar outlined. Note, the plane of the hydrofoil is highlighted in orange in (a) and (b). (d) A schematic of the hydrofoil's TE represented as a cantilever with a linear load declining towards the TE tip.

of a HATT blade, it can represent a segment of a blade in isolation. Using this simplification, focus can be given to evaluating the morphing mechanisms and their fundamental operation.

A NACA 0012 foil geometry was chosen for its symmetric profile, which is typical of VATT blades [11,14,18,19]. As HATT blades utilise cambered hydrofoils for their increased lift [4,6,9,16,17], the influence of camber is investigated with full-scale simulations in section 3.2.2.

In this study, the latter two thirds of the chord length were assigned as the TE, with the leading edge (LE) supported by a rigid spar, as illustrated in Fig. 1(c). In designing a morphing TE, an initial approach is to treat it as a single cantilever beam with a distributed load that is declining linearly from the spar to the TE tip [12], as shown in Fig. 1(d). In such a case, the maximum deflection, δ [m], is given by the following equation [21],

$$\delta = \frac{ql^4}{30EI},$$ (1)

Table 1
Mechanical properties of the flexible UD-GF/Epoxy.

Material property [units]	Mean value ± standard deviation
Longitudinal tensile modulus, E_1^T [GPa]	30.0 ± 1.2
Longitudinal tensile strength, X_T [MPa]	577 ± 30
Transverse tensile modulus, E_2^T [MPa]	117 ± 7
Transverse tensile strength, Y_T [MPa]	4.72 ± 0.23
In-plane shear modulus, G_{12} [MPa]	89.8 ± 1.8
In-plane shear strength, S [MPa]	3.38 ± 0.20
In-plane Poisson's ratio, ν_{12} [-]	0.30 ± 0.03

where q is the declining distributed load [N/m], l is the length of the TE [m], E is the Young's modulus [GPa], and I is the second moment of area [m^4].

Conventionally, the chord length of the blade is determined by a hydrodynamic analysis [17], while the applied load is a function of the relative water velocity and pressure coefficient [12]. For a morphing blade, the pressure coefficient is coupled to the deflection of the TE, so the Young's modulus and second moment of area are the only remaining variables that can be used to control the deflection. Many morphing TE designs are based on tailoring one or both of these stiffness properties [22].

For initial TE design evaluation, three concepts were considered:

1. Closed TE with compliant composite skins – a conventional design with a high geometric stiffness and low material stiffness.
2. Open TE with compliant composite skins – the geometric stiffness is greatly reduced by opening the TE.
3. Closed TE with corrugated composite skins – the geometric stiffness of the skins is reduced to further increase their compliance.

The rationale for these three concepts is discussed further in Appendix A. In addition to assessing the passive morphing mechanism, the initial design evaluation was also used to investigate the key design parameters and assess manufacturability. Later in the study, the material response of a full-scale TE will be considered using numerical simulation.

2.2. Materials

In this study, two composite material systems were considered: the first was a flexible composite material used for simulation and testing of lab-scale prototypes (approx. 1/6th scale – further details of which are provided in sections 2.3.1 and 2.4); the second was a stiff composite material for simulation of full-scale blades. Flexible composites were necessary due to the operating limits of the test flume, i.e., during initial trials it was observed that the water velocity was insufficient to morph a prototype blade made from conventional, stiff composites. As such, a 646 g/m^2 unidirectional glass fibre (UD-GF) reinforcement (from Ahlstrom-Munksjö) was infused with EF80 flexible epoxy resin (from Easy Composites Ltd. [23]). The resulting laminate was mechanically tested to determine its properties; the details of which are given in the sections that follow. For the full-scale simulations, a UD-GF/powder-epoxy system was chosen due to its suitability for manufacturing thick wind and tidal turbine blades [24–26] and its well-documented mechanical properties [27].

2.2.1. Test specimen manufacturing
Flexible UD-GF/Epoxy laminates were manufactured using a standard vacuum infusion process (VIP). All infusions were performed at room temperature and left to cure at room temperature for 48 h. Subsequently, the test laminates were postcured in accordance with the recommendations of the technical data sheet [23], i.e., 1 h at 40 °C, 1 h at 60 °C, and 3 h at 80 °C. GF/Epoxy end tabs were bonded to the test panels using Araldite® Rapid adhesive. All test coupons were extracted by means of a water-lubricated diamond-coated saw blade and then dried in a convection oven at 50 °C for 24 h prior to testing.

2.2.2. Mechanical test methods
Uniaxial tensile tests were conducted in accordance with ASTM D3039 [28] to determine the longitudinal and transverse tensile properties of the flexible UD-GF/Epoxy composite. Additional uniaxial tests were performed in accordance with ASTM D3518 [29] to determine the in-plane shear properties. Longitudinal and in-plane shear specimens were tested using a 300 kN test machine (MTS Criterion, model 45) with a 250 kN load cell, while transverse specimens were tested using a 50 kN

Table 2

Mechanical properties of the UD-GF/powder-epoxy, taken from [27].

Material property [units]	Mean value $\pm$ standard deviation
Longitudinal tensile modulus, E_1^T [GPa]	39.7 $\pm$ 1.5
Longitudinal tensile strength, X_T [MPa]	782 $\pm$ 36
Longitudinal compressive modulus, E_1^C [GPa]	37.9 $\pm$ 0.7
Longitudinal compressive strength, X_C [MPa]	643 $\pm$ 10
Transverse tensile modulus, E_2^T [GPa]	11.9 $\pm$ 0.2
Transverse tensile strength, Y_T [MPa]	46.5 $\pm$ 2.2
Transverse compressive modulus, E_2^C [GPa]	14.0 $\pm$ 0.5
Transverse compressive strength, Y_C [MPa]	185 $\pm$ 10
In-plane shear modulus, G_{12} [GPa]	3.67 $\pm$ 0.04
In-plane shear strength, S [MPa]	53.7 $\pm$ 0.3
In-plane Poisson's ratio, ν_{12} [-]	0.29 $\pm$ 0.14

test machine (Instron 3369) with a 1 kN load cell. An Imetrum video extensometer was used to measure strain for each test via digital image correlation (DIC). In each case, at least 5 specimens were tested.

2.2.3. Mechanical properties

The mechanical properties of the flexible UD-GF/Epoxy are given in Table 1. As expected, the transverse modulus of the composite is significantly lower than the longitudinal modulus. It should be noted that the in-plane shear strength, S, represents the maximum shear stress at 5 % shear strain, in accordance with ASTM D3518 [29]. Representative force–displacement curves are given in Appendix C – Supplementary material; Fig. C1–Fig. C3. Although the compressive properties of the flexible UD-GF/Epoxy were not determined, the tensile properties were sufficient for evaluation of the lab-scale prototypes. For the full-scale simulations, the mechanical properties of UD-GF/powder-epoxy are provided in Table 2.

2.3. Numerical simulation

Two sets of numerical simulations were performed:

Simulation of the three TE designs described in section 2.1. These simulations were performed for lab-scale models (i.e., approx. 1/6th scale) for comparison with lab-scale testing.

Simulation of a full-scale TE design; down-selected from the three designs mentioned above.

2.3.1. Lab-scale prototype design

A 3D shell model of a blade was created in Abaqus FEA by importing a NACA 0012 foil and extruding it along the z-axis. In the case of the corrugated model, corrugations were added to the foil geometry prior to extrusion. The blade model was given a span of 300 mm and a chord length of 150 mm – these dimensions were based on the allowable dimensions for flume testing (see section 2.5). The resulting model was partitioned into a LE, a TE, and a rigid spar as illustrated in Fig. 1(c). These sections were prescribed composite lay-ups of flexible unidirectional GF/Epoxy; $[0_2]$ for the LE and $[0]$ for the TE, where the fibres were aligned spanwise (z-direction). This lay-up was chosen to maximise the spanwise stiffness and minimise the chordwise TE stiffness. This lay-up, in combination with the flexible composite, was required due to the pressure distribution over the chord of the blade, i.e., the pressure acting on the TE is relatively low (see Fig. 2(a)) and a high degree of compliance was necessary for morphing. Each ply was given a thickness of 0.5 mm and a density, ρ, of 1800 kg/m^3. Note, the corrugated model assumed that an isotropic, elastomeric material ($E = 0.2$ MPa, $\nu = 0.45$, $\rho = 1050$ kg/m^3) was used as a skin (0.5 mm thick) between the corrugations. For each design, the rigid spar section was kinematically coupled to a reference point with encastre boundary conditions, thus, fixing it in space.

A dynamic, implicit analysis step was created to apply blade loads and determine the resulting deformation. Conventionally, the loads are calculated for each blade segment using blade element momentum theory (BEMT) and then applied either as point loads at the hydrodynamic centre [9], surface traction distributions across the spar caps [4,17], or uniform distributions across the whole hydrofoil section [16]. In the case of morphing blades, however, these methods are insufficient for fully resolving the hydrofoil's chordwise deformation. Instead, the pressure distribution along the chord had to be determined for a given hydrofoil geometry, and then updated as the hydrofoil deformed. For this study, XFOIL [30] was used to generate the pressure coefficient (C_P) distributions shown in Fig. 2(a).

For both the simulations and experiments, a 30 s ramp in water
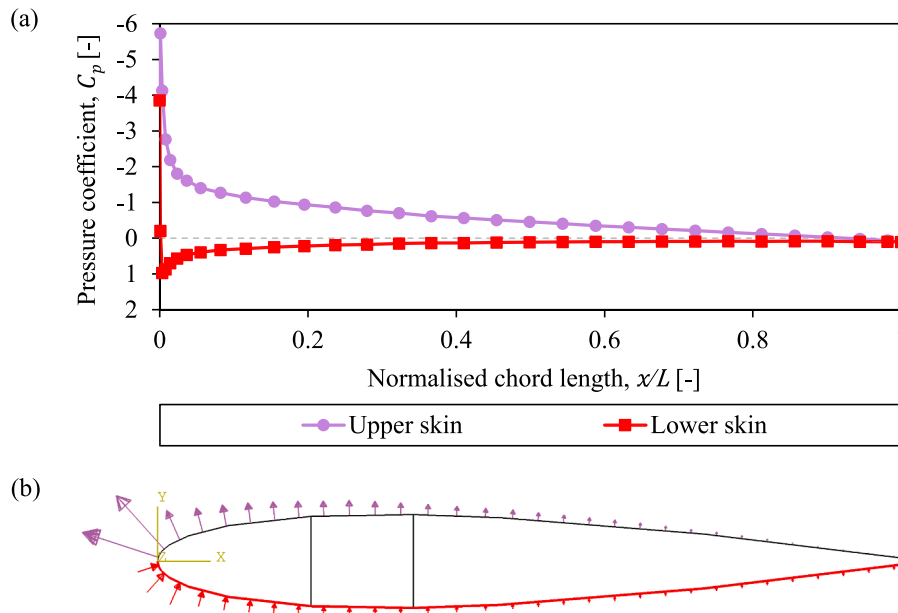
Fig. 2. (a) The pressure coefficient distributions along the chord of the hydrofoil. (b) The hydrofoil model in Abaqus FEA, with the pressure distributions applied as mapped analytical fields across the upper and lower skins (indicated by purple and red arrows, respectively).

Table 3
Conditions for simulation of the prototype blades.

Parameter [units]	Value
Water density, ρ_∞ [kg/m^3]	998
Freestream water velocity, V_∞ [m/s]	0 – 0.5
Kinematic viscosity of water [m^2/s]	1e-6
Speed of sound in water [m/s]	1480
Initial angle of attack, α_0 [°]	10

velocity was used to load the blades, i.e., zero to final velocity in 30 s. Assuming this ramp equated to half an oscillating wave, it can be said that the loading had a frequency, $f = 1/2(30) = 0.0167$ Hz.

In aerodynamics/hydrodynamics, the reduced frequency, k, is a non-dimensional parameter used to indicate the unsteadiness of the loading conditions,

$$k = \frac{\pi f L}{V_\infty}, \tag{2}$$

where L is the chord length [m], and V_∞ is the freestream velocity [m/s].

Generally, the flow is unsteady when $k > 0.05$ and highly unsteady when $k > 0.2$ [31].

For the lab-scale prototype, $L = 0.15$ m and $V_\infty = 0.5$ m/s, resulting in $k = 0.0157$. As $k < 0.05$, the flow was quasi-steady and hence the steady flow analysis with XFOIL was appropriate. Additionally, it is reported elsewhere that the use of XFOIL with a quasi-steady assumption provides a good prediction of loadings on tidal turbine blades [32,33].

The resultant pressure on the hydrofoil, P [Pa], was calculated using the following equation [34],

$$P = C_P \left(\frac{1}{2}\rho_\infty V_\infty^2\right) + P_\infty, \tag{3}$$

where ρ_∞ is the water density [kg/m^3], and P_∞ is the freestream pressure [Pa]. The values used for Equation (2) are given in Table 3.

In initial analyses, it was assumed that the internal pressure and freestream pressure would cancel each other due to the tidal turbine blade being fully flooded. As will be discussed in section 3.1, however, this assumption did not hold true for the prototype testing. Consequently, an internal-external pressure difference was accounted for in
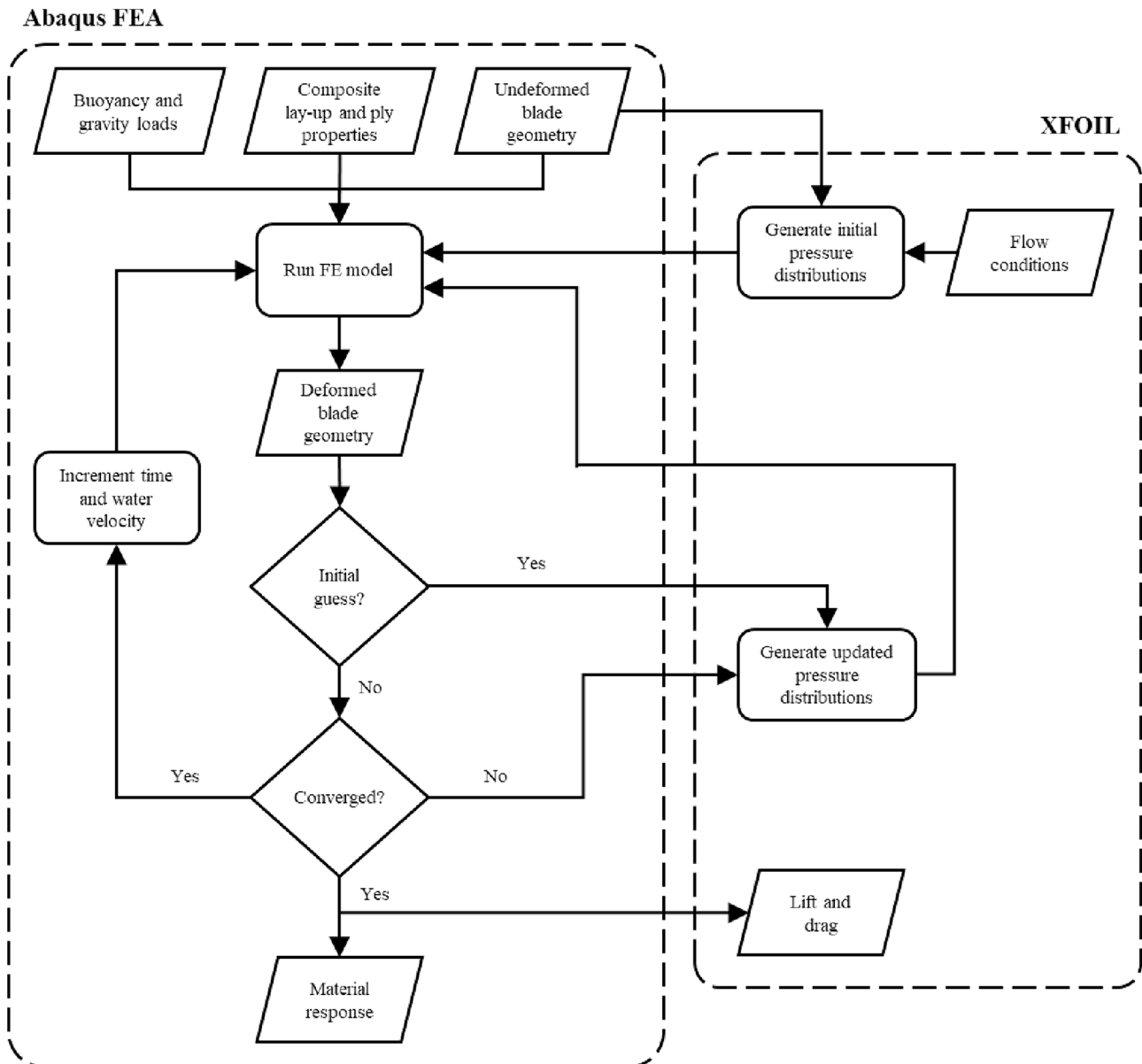
Fig. 3. Flowchart for the numerical simulation algorithm using Abaqus FEA and XFOIL.
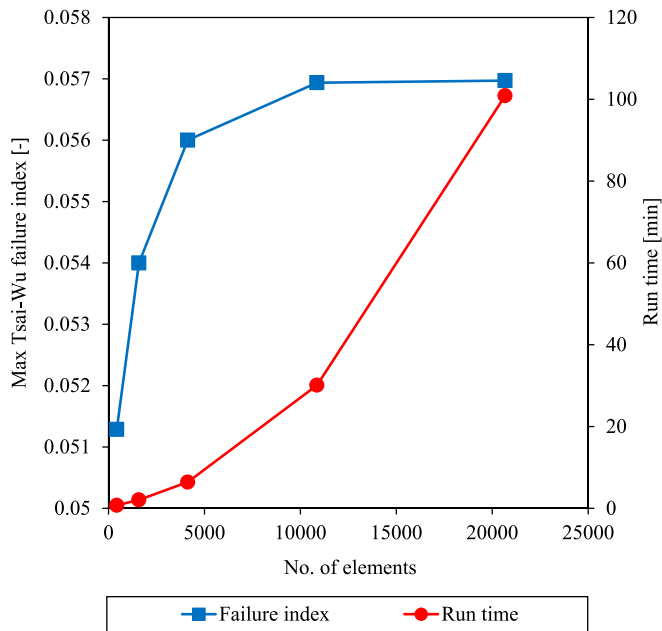
Fig. 4. Results of the mesh convergence study. The maximum Tsai-Wu failure index was used as the convergence criterion. Note, the run time shown is that of the final model, i.e., it does not include the iterative process required to balance the morphing deformation and the change in pressure distribution.

later simulations.

As shown in Fig. 2(b), the pressure distributions were applied to the 3D shell model as pressure loads via mapped analytical fields. In addition, a gravitational load, F_G [N], and a buoyancy load, F_B [N], were applied to the blade model; the latter was calculated via the Archimedes' principle and applied as a body force,

$$F_B = \rho_\infty \varphi g, \tag{4}$$

where φ is the volume of the composite [m^3] and g is acceleration due to gravity [m/s^2].

As contact between the TE skins was anticipated, a default surface-to-surface contact interaction was included in the model.

The model was solved in at least six analysis steps, with the water velocity increased incrementally. For each increment, the corresponding pressure loads were determined using XFOIL and input into Abaqus FEA to predict the TE deformation. To balance the deformation and pressure change, the deformed hydrofoil coordinates were imported back into XFOIL to update the pressure distributions, and this process was iterated within the time step until the solution converged as shown in Fig. 3. Frequently, convergence required up to 10 iterations, but this varied for each analysis step and model.

Finally, a mesh convergence study was performed (see Fig. 4); the model was meshed using 4-noded, quadrilateral, stress/displacement shell elements with reduced integration and large-strain formulation (i. e., S4R). Note, the run time provided in Fig. 4 refers to the run time of the final model solution, however, the total iterative process took much longer to complete e.g. depending on the model and the number of iterations required, a mesh of 4130 elements required circa 4 h to complete. As a reasonable compromise between accuracy and run time, a mesh of 4130 elements was chosen for all simulations. Note, an Intel Core i7 PC with 32 GB of RAM was used for all simulations.

2.3.2. Full-scale design

For the full-scale simulations, several notable changes were made to the model described in the previous section. The first and most obvious difference was in relation to scaling. The chord length was increased to 0.85 m, which was representative of a full-scale VATT [13]. While the

chord length of HATT blades typically vary along the span, 0.85 m was representative of the chord length between the mid-span and the tip of the blade [16,17]. The maximum water velocity was also increased to 5 m/s, which is within the typical range assumed for the relative velocity of full-scale blades [13,16,17]. With $L = 0.85$ m and $V_\infty = 5$ m/s, the reduced frequency for the full-scale simulations was $k = 0.0089$, which was again quasi-steady.

A second difference was the addition of two shear webs to create a box spar, which provided a more accurate representation of a full-scale blade [4]. Both ends of this box spar were given encastre boundary conditions.

A third difference was the use of UD-GF/Powder-epoxy and the investigation of various composite lay-up configurations. Several lay-up configurations were considered for the morphing TE, the details of which will be discussed in section 3.2. In each case, the general lay-up configuration of each was extended to the rest of the blade (i.e., the LE and box spar). As the morphing TE provided little load-bearing capacity, the LE and box spar were considered the main load-bearing components. For this reason, they were given a conservative ply count of 16 plies, which was sufficiently rigid for all simulated design cases (i. e., no significant deformation of the LE or box spar was predicted). While a detailed study of the box spar-TE transition was outside the scope of this study, it was assumed that it would require additional reinforcement to resist the peeling stresses induced by morphing. As such, two additional plies of composite were added to the transition, which extended 0.1 m along the TE. Both plies were given 90° orientations to align the fibres in the chordwise direction.

A final difference was the modification of the NACA 0012 geometry to investigate the use of camber for increasing the initial angle of attack, α_0. In this instance, the term "camber" is used to describe asymmetry in the initial hydrofoil design rather than asymmetry due to morphing during operation, i.e., at time = 0, the hydrofoil has a camber, which gives it a higher initial angle of attack than the NACA 0012 hydrofoil with $\alpha_0 = 10°$. The cambered geometry was created by allowing the lab-scale open TE hydrofoil to deform under self-weight until it reached a desired angle of attack. This deformed geometry was exported from Abaqus FEA, scaled, and then imported back into Abaqus FEA for analysis. In this way, two cambered hydrofoils were created with $\alpha_0 \approx 14°$ and $\alpha_0 \approx 18°$. Further details of the cambered hydrofoils are given in section 3.2.2.
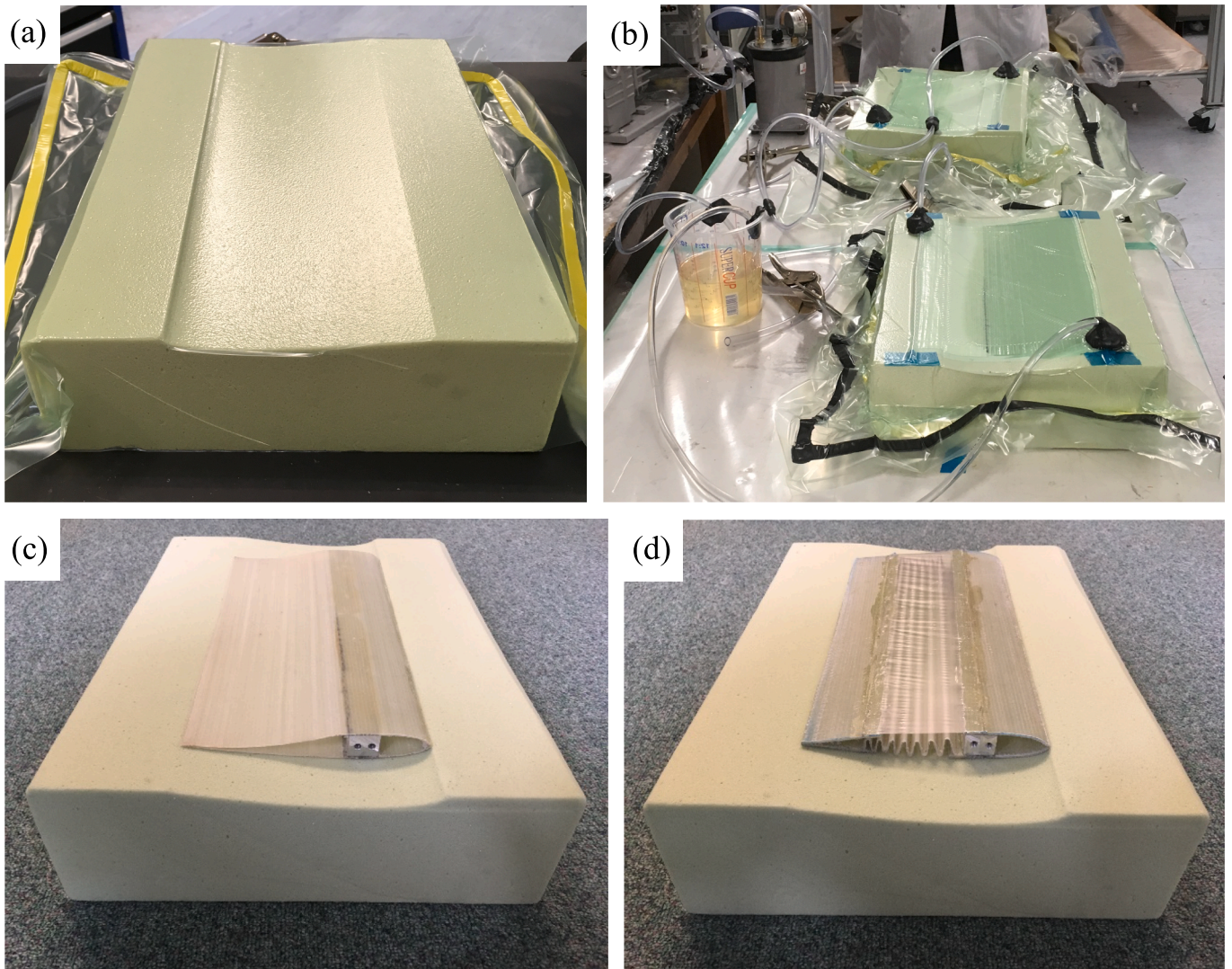
2.4. Prototype blade manufacturing

To aid in evaluating the TE designs, lab-scale prototype blades were manufactured for flume testing. The blade skins were manufactured using two female moulds machined from high-density polyurethane (HDPU) foam blocks. As shown in Fig. 5(a), the moulds were vacuum bagged to form a smooth mould surface; similar to the method used by Vos et al. [35] for manufacturing a morphing wing. Infusion was performed using the VIP technique (Fig. 5(b)). As with the numerical model, two plies of UD-GF were used for the LE, while one ply was used for the TE. In each case, the 0° fibres were aligned in the spanwise direction. Each ply had a thickness of approximately 0.5 mm.

Prototype blades with a span of 0.3 m were assembled by adhesively bonding the skins to an aluminium spar using Araldite® Standard. For the closed TE blade, the skins were bonded together at the LE and TE. For the open TE blade, shown in Fig. 5(c), the skins were left unbonded at the TE.

For the corrugated TE, a 3D printed polylactic acid (PLA) mould was used to manufacture corrugation via VIP (the mould and corrugation are shown in Fig. C.4 in Appendix C – Supplementary material). The corrugated section was then adhesively bonded to the LE, as well as a TE tip. To create a flexible skin for the corrugation, a thermoplastic polyurethane film (25 μm thick) was adhesively bonded between the LE and the TE tip. The resulting prototype blade is shown in Fig. 5(d).

Fig. 5. (a) The mould used to manufacture blade skins. (b) The glass-fibre skins being infused with flexible epoxy. (c) A prototype blade after the skins have been bonded to the aluminium spar. This blade had an open TE. (d) A prototype blade with a corrugated TE.

2.5. Flume testing

The prototype blades were tested in a water tunnel with a test section of 2 m × 0.4 m × 0.33 m (length × width × depth). The prototype blades were positioned at a depth of 0.165 m. The aluminium spar of each blade was bolted to transparent side supports (acrylic sheet), which fixed the blade at an initial angle of attack of 10°. The gap between the ends of the blade and the acrylic sheet was not water-tight (approx. 1 mm gap), so water was able to enter inside the blades during the mounting process and during testing. To match the design conditions, the current in the flume was ramped to a freestream velocity of approx. 0.5 m/s during tests. The TE deflection of each prototype blade was recorded using a CCD IMPREX 50MP camera with a resolution of 2056 × 2060 pixels, capturing the physical dimension of 0.19 m × 0.19 m at a frame rate of 10 frames per second. For each TE design concept, only one prototype blade was tested in the flume. Naturally, this does not capture any manufacturing variability that may occur across the production of multiple blades, however, each blade was of sufficient quality to provide representative behaviour for down-selection purposes.

3. Results and discussion

In this section, the results of lab-scale tests and simulations are presented and analysed in the context of structural, material, and hydrodynamic performance. Following this initial evaluation, a suitable flexible TE design is identified for further simulated analysis at full-scale. The full-scale analyses consider the effect of composite lay-up configuration, the effect of blade camber, and the potential for bend-twist coupling of the blade skins. Finally, consideration is given to future work in this area.

3.1. Evaluation of trailing edge designs

A comparison of simulation and experiment for each prototype TE design is shown in Fig. 6. Morphing was achieved in each case with varying degrees of success.

For the closed TE (Fig. 6(a)), morphing caused the bottom skin to go into tension and the top skin into compression, causing the latter to buckle. While designed buckling can be a useful mechanism for morphing structures (i.e., for nonlinear "snap" changes in structure) [36], uncontrolled buckling is considered one of the primary means of turbine blade failure [37]. In particular, trailing edge failure in conventional designs is often driven by buckling under edgewise loads, which can subsequently lead to adhesive debonding [38,39]. As such, the uncontrolled buckling of the closed TE design was undesirable and represented a structural failure, which could also lead to hydroelastic
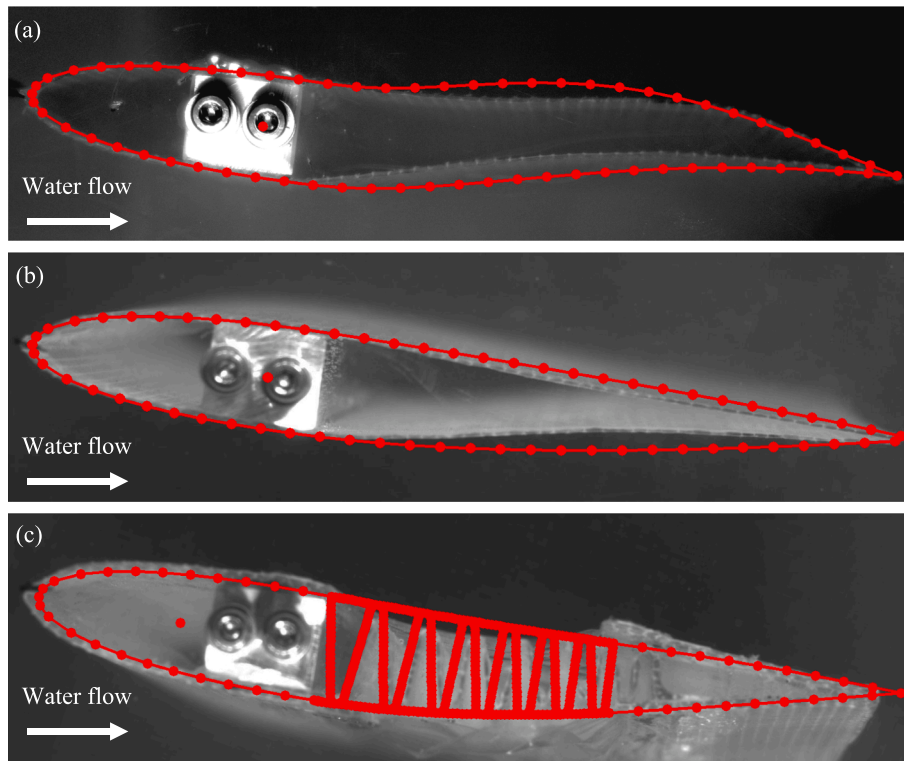
Fig. 6. Comparison of experimental results and simulated results (red lines) for the three TE designs: (a) closed TE; (b) open TE; (c) corrugated TE.

instabilities [40,41] or localised material failure [38]. With respect to the latter, it was not possible to accurately determine the likelihood of failure because the compressive strength of the flexible GF/Epoxy was not measured. Nevertheless, plotting the maximum simulated tensile strain against the change in angle of attack, $\Delta\alpha$ [°], confirmed that the buckling would have a negative impact on the material (see Fig. 7), with four times higher strain for the closed TE. Naturally, these strains would be expected to increase further for the full-scale designs because thicker TE skins will undergo higher bending strains for equivalent deformation.

As shown in Fig. 6(b), the open TE design was able to achieve morphing without buckling, resulting in a comparatively low maximum tensile strain (Fig. 7). This was because the skins were free to deflect independently, allowing the top skin to slide over the bottom skin without being forced into compression. One notable discrepancy between simulation and experiment was the difference in TE chord thickness (i.e., the distance between the top and bottom skin). This discrepancy will be revisited later in this section.

In the case of the corrugated TE design (Fig. 6(c)), morphing was achieved, but with several caveats. The first was that the design consisted of a single corrugation, not two corrugated skins, as initially envisioned. This was due to the scale of the prototype, which limited the range of geometric parameters for the corrugation. Initial simulations showed that skin buckling persisted for small corrugations, while increasing the height of the corrugation eventually caused the top and bottom skins to contact each other. Note, the results of these initial simulations are provided in Fig. C5 in Appendix C – Supplementary material. Consequently, it was easier to manufacture the trailing edge as a single, tall corrugation, similar to the morphing wing developed by Yokozeki et al. [42]. Despite this simplification, another disadvantage of the corrugated design was the comparative complexity of manufacturing it. Again, due to scale, conforming the GF fabric and bagging materials to the acute angles of the corrugated mould was challenging. Another manufacturing challenge was the inclusion of elastomeric skins. While it was possible to bond polyurethane film to the composite skins, it did not maintain a smooth hydrofoil surface during flume testing; a problem

that is considered one of the main drawbacks of corrugated skins [43].

While many of the challenges with the corrugated TE design were due to manufacturing complications at the lab scale, this concept still introduced more complexity to the design and manufacturing process than the open TE design. For example, little is known about how the composite-elastomer interface would perform in high cycle fatigue, or what effect marine conditions would have on it [43]. Given that cost and reliability are paramount for the tidal energy industry, the simplicity of the open TE design should be more attractive for turbine developers. For this reason, it was selected for further analysis.

Initially, TE deflection was to be assessed under steady state conditions at 0.5 m/s, however, it became apparent that an unexpected partial collapse of the TE was occurring as the water velocity was being ramped. This collapsing phenomenon is shown in Fig. 8. Revisiting the model assumptions, it was clear that this phenomenon was not accounted for by the pressure distributions generated in the XFOIL analysis; shown in Fig. 9. Rather, as the freestream pressure, P_∞, in Equation (2) was increased from zero, it was found that the simulated deformation approached that of the experiments. This suggested that a hydrostatic pressure difference existed between the freestream water and the water within the flooded blade, and that it increased as a function of water velocity.

As precise water velocity data was not measured for this transient stage, it was fitted to the modelled deformation. This produced a linear trend, with $V_\infty = 0.25$ m/s after approx. 30 s (see Fig. 10). This trend was in agreement with another study [15] that observed the same flume reaching steady state after approximately 1 min. Similarly, it was possible to fit the internal-external pressure difference to the deformation of the prototype blade (Fig. 8), which produced a linear relationship as a function of water velocity (see Fig. 11). The slope of this relationship initially matched well with the average pressure acting on the upper skin. This suggested that the internal pressure of the TE may have been equalising with the low pressure side of the blade, possibly via the open ends of the TE. The trends diverge at higher water velocities, suggesting other hydrodynamic effects may play a role. While a detailed analysis of
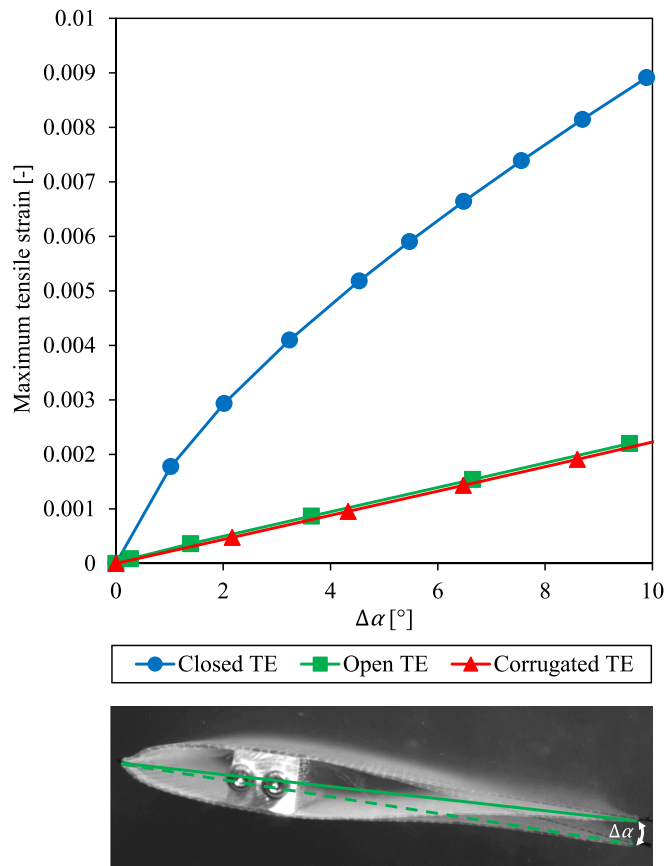
Fig. 7. (Top) The maximum tensile strain for each simulated TE design as a function of the change in the angle of attack. (Bottom) Overlapping images of the open TE prototype show the change in angle of attack. Dashed and solid lines represent the chord line before and after morphing, respectively.

this phenomenon was outside the scope of the current work, the linear relationship of water velocity and internal-external pressure difference was assumed as the basis for determining the internal-external pressure difference of the full-scale blades.

As can be seen from Fig. 12, the partial collapse of the TE caused an increase in the maximum simulated tensile strain compared to the idealised case with no internal-external pressure difference. Nevertheless, there was still a significant factor of safety for this design, as the mean transverse tensile failure strain for the flexible UD-GF/Epoxy was 0.044. Revisiting the pressure coefficient distributions in Fig. 8, it can also be seen that, despite the partial collapse, the morphing mechanism was effective in significantly altering the hydrodynamic response of the blade. The interested reader can find a visualisation of the morphed geometries overlaid with the pressure coefficient distributions in Fig. C6 in Appendix C – Supplementary material.

3.2. Simulations of full-scale open trailing edge designs

3.2.1. Effect of lay-up configuration

From the lab-scale testing and simulations, it was unclear whether the collapsing phenomenon could be prevented by tailoring the skin stiffness. Increasing the open TE prototype's skin thickness from 1 ply to 2 plies resulted in a semi-rigid blade that neither collapsed nor morphed. This was due to the cubic relationship between skin thickness and the second moment of area (see Eq. (A.1), Appendix A). As such, it was adjudged that the effect should be re-investigated at full-scale, where incremental changes in skin thickness were more feasible.

As previously mentioned, UD-GF/Powder-epoxy was chosen for the full-scale simulations. While the compliance of the flexible UD-GF/

Epoxy was required at lab scale, the robust mechanical properties of UD-GF/Powder-epoxy were preferred due to the magnitude and variety of loads that full-scale blades undergo (e.g. bending, torsion, fatigue, impact, etc.). It was also necessary to consider the effect of lay-up configuration due to the importance of fibre orientation in resisting various load cases. In Fig. 13, a "rigid" blade (i.e., closed TE) with a quasi-isotropic (QI) lay-up is shown as a reference alongside three open TE blades with the following lay-ups: biaxial $[90/0]_{2S}$, triaxial $[\pm 45/0_2]_S$, and QI $[90/\pm 45/0]_S$. In each case, the 0° fibres were aligned in the spanwise direction (z-direction) and each ply was given a thickness of 0.5 mm.

The Tsai-Wu failure index was used to compare the various composite lay-up configurations,

$$F_1 \sigma_{11} + F_2 \sigma_{22} + F_{11} \sigma_{11}^2 + F_{22} \sigma_{22}^2 + F_{66} \tau_{12}^2 + 2F_{12} \sigma_{11} \sigma_{22} = 1, \qquad (5)$$

where σ_{11} is the normal stress in the longitudinal direction, σ_{22} is the normal stress in the transverse direction, and τ_{12} is the in-plane shear stress. The Tsai-Wu parameters are defined using the strengths provided in Table 2,

$$F_1 = \frac{1}{X_T} - \frac{1}{X_C}, \ F_2 = \frac{1}{Y_T} - \frac{1}{Y_C}, \ F_{11} = \frac{1}{X_T X_C}, \ F_{22} = \frac{1}{Y_T Y_C}, \ F_{66} = \frac{1}{S^2}, \qquad (6)$$

except for the biaxial strength interaction parameter, F_{12}, which requires an additional fitting coefficient, F_{12}^*,

$$F_{12} = F_{12}^* \sqrt{F_{11} F_{22}}. \qquad (7)$$

The Tsai-Wu failure index is one of the most commonly used composite failure criteria due to its increased ability to fit to experimental data [44]. Provided sufficient test data is available, this enables better biaxial strength predictions compared to other in-built composite failure criteria available in Abaqus FEA e.g. maximum strain theory, Tsai-Hill theory, etc [45]. However, the biaxial strength interaction parameter can be difficult to measure experimentally. As an alternative, Tsai and Hahn [46] recommended generalising the failure criterion by setting F_{12}^* = -0.5, which is the approach taken in the current study.

As can be seen, no cases are predicted to result in failure, and all have a factor of safety of 8 or more. It was notable that the location and magnitude of maximum failure index changed depending on TE design and lay-up configuration. For the "rigid" blade, the max failure index concentrated at the TE tip where the top and bottom skins met. For the open TE designs, the max failure index transitioned back along the TE towards the box spar, as was expected for the cantilevered skins. It should also be noted that all three full-scale open TE blades achieved morphing without collapsing. This showed that, under the assumed conditions, collapsing was not a precondition of morphing and a compromise could be found for the skin stiffness.

Although the triaxial lay-up gave greater flexibility to the TE than the biaxial and QI lay-ups (see Fig. 14), it also resulted in a doubling of the maximum failure index due to the absence of fibres oriented in the chordwise direction. Given the similar performance of the biaxial and QI lay-ups, load cases beyond chordwise bending should be considered, i.e., flapwise bending, edgewise bending, and torsion. Detailed analysis of such load cases were beyond the scope of the current work, however, other studies have favoured QI skins for tidal turbines due to the multi-axial loading they undergo [16,17]. Much in the same way that ± 45° plies give torsional resistance to the shear webs of a blade, the presence of ± 45° plies in QI laminates makes them stronger and stiffer than biaxial cross-ply laminates in torsion. Given that open TEs already have significantly lower torsional stiffness than closed TEs [35], it was decided that an open TE design with a QI lay-up would provide a balanced compromise between geometric compliance and material robustness.
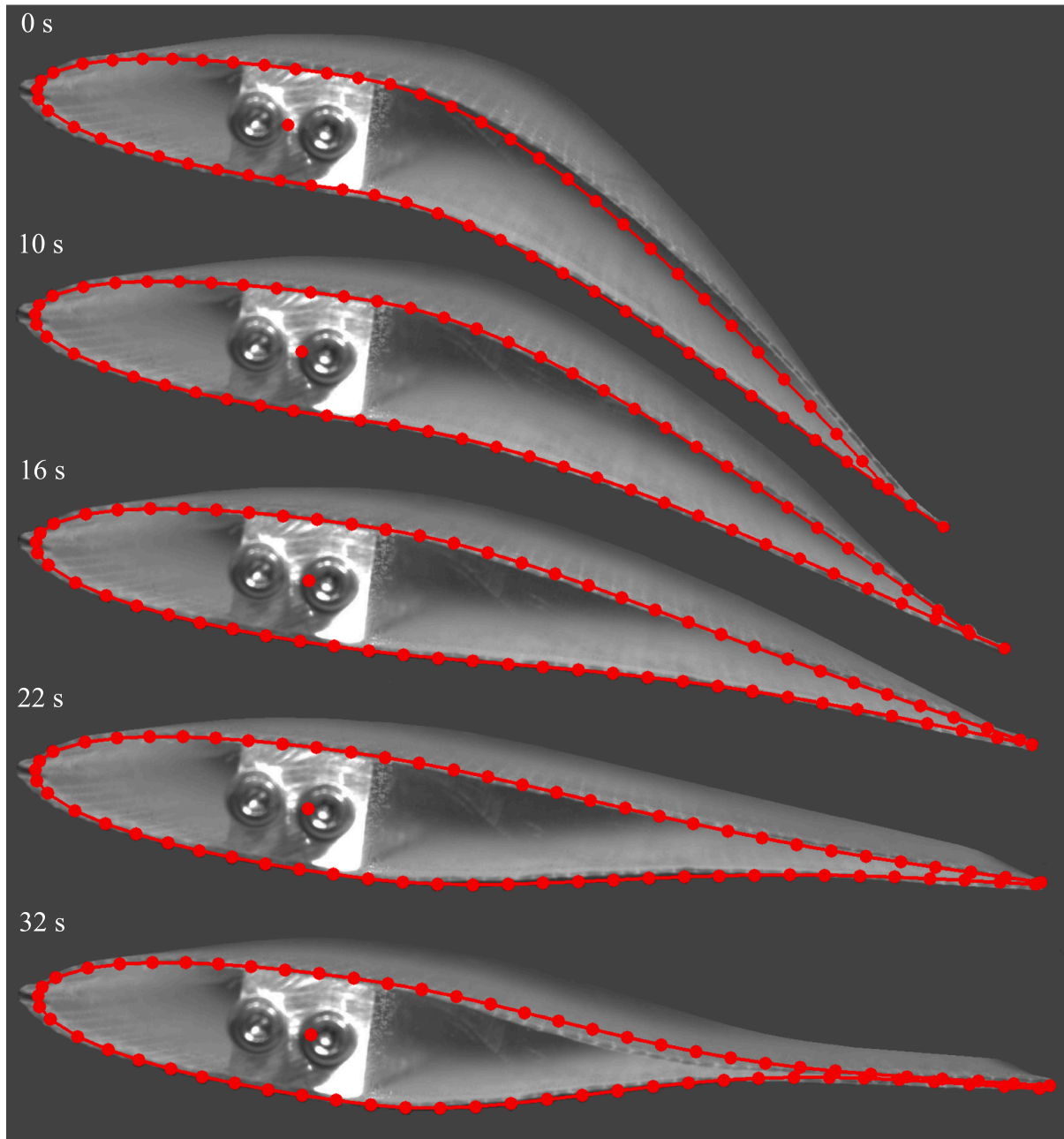
Fig. 8. Comparison of the open TE experiment and a fitted simulation at various time steps (note, the water velocity was 0 m/s at 0 s). Initially, the blade was deformed by its own weight. As the water velocity increased with time, the angle of attack changed and the TE thickness decreased.

3.2.2. Effect of camber

As cambered blades are typically chosen for HATTs [17], it was worthwhile considering how they could be implemented with an open TE design, and what were the limitations of this. Two cambered blades were created for comparison with the original symmetric blade (i.e., NACA 0012 with $\alpha_0 = 10°$). Each of these blades was given a camber that altered its initial angle of attack; $\alpha_0 \approx 14°$ and $\alpha_0 \approx 18°$. To ensure a fair comparison of the blades, the skin thickness of each cambered blade was iterated until the final angle of attack was approximately the same as that of the original symmetric blade (i.e., $\alpha \approx 8°$). For $\alpha_0 \approx 14°$ and $\alpha_0 \approx 18°$, the skin thicknesses were 2.88 mm and 2.48 mm, respectively. The deformation of the TE, shown in Fig. 15, demonstrated the sensitivity of the design to variation in skin thickness. Similar sensitivity has been reported for other morphing structures [7]. Although morphing was achieved in each case, it was evident that TE collapse began to occur

again as the skin thickness decreased. Nevertheless, the effect was only severe in the case where $\alpha_0 \approx 18°$ (Fig. 15(c)).

In terms of material performance, the larger deformation of the cambered blades resulted in higher stresses in the blade skins and, consequently, higher failure indices, as can be seen in Fig. 16. Note, the change in angle of attack, $\Delta\alpha$, was plotted relative to the initial angle of attack of the original symmetric blade ($\alpha_0 = 10°$). As such, the cambered blades are shown as initially having a negative $\Delta\alpha$.

Interestingly, the slope of the curves in Fig. 16 decreased as the camber increased. This was due to the thinner TE skins of the cambered blades, i.e., from beam bending theory, stress increases with increasing distance from the neutral axis [21]. As a result, the large increase in deformation for the cambered blades produced a modest increase in the failure index, i.e., for $\alpha_0 \approx 14°$, a 200 % increase in $\Delta\alpha$ resulted in a 75 % increase in the max failure index, while, for $\alpha_0 \approx 18°$, a 400 % increase in
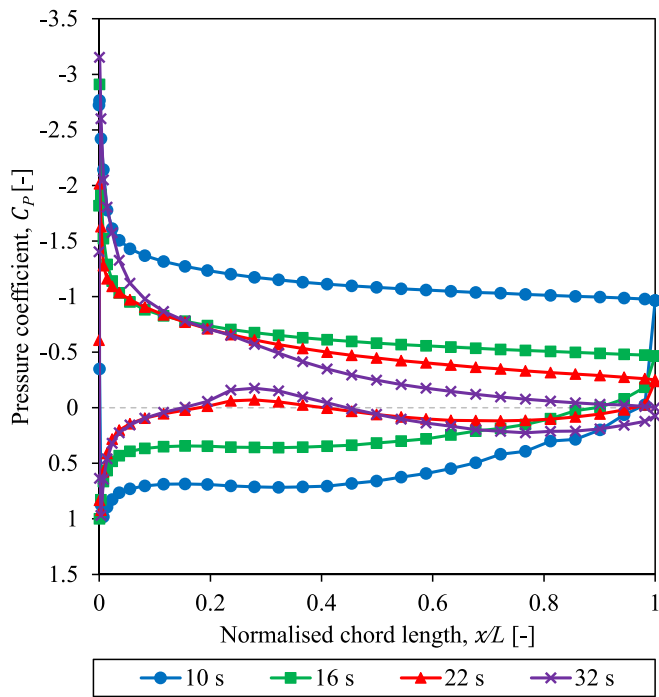
Fig. 9. Pressure coefficient distributions from the XFOIL analysis. The curves correspond to the time steps given in Figure 8, i.e., 10 s, 16 s, etc.
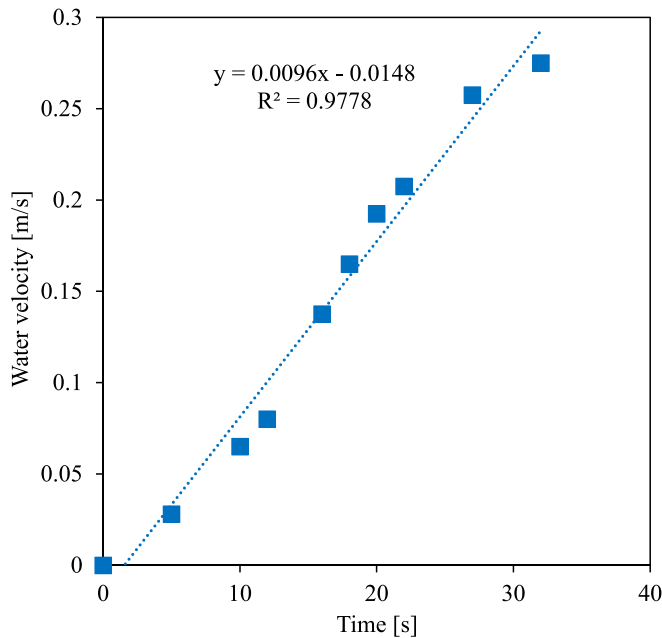

Fig. 10. Fitted water velocities for the flume tests (linear fit in dashed blue).

Fig. 11. Pressure differences acting on the open TE prototype as a function of water velocity. The internal-external pressure difference was fitted linearly (dashed blue line). This linear fit also correlated with the low pressure side of the blade (i.e., the upper skin) at low water velocities.

Fig. 12. Maximum strain for the open TE model with and without an internal pressure difference. The partial collapse of the TE resulted in a higher strain.

$\Delta\alpha$ resulted in a 160 % increase in the max failure index. Moreover, the max failure index for the cambered blades showed that the morphing mechanism still had a relatively large factor of safety.

To compare and evaluate the hydrodynamic performance of the blades, the lift coefficient, C_L, was plotted against $\Delta\alpha$ (see Fig. 17). The C_L of each blade followed a similar decreasing trend as they morphed. This drop-off in C_L represented the fundamental function of the passively morphing TE; to reduce the load transmitted through the blades as a function of the operating conditions. The cambered blades counterbalanced the dec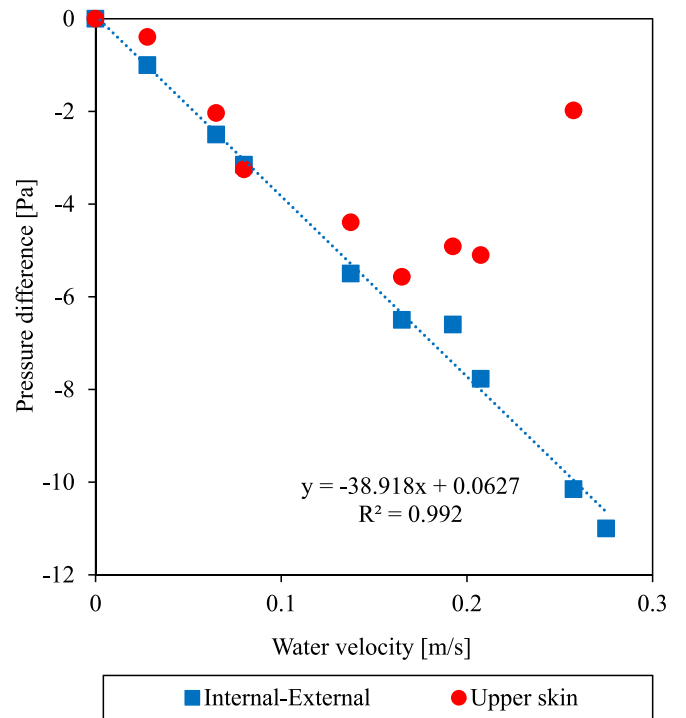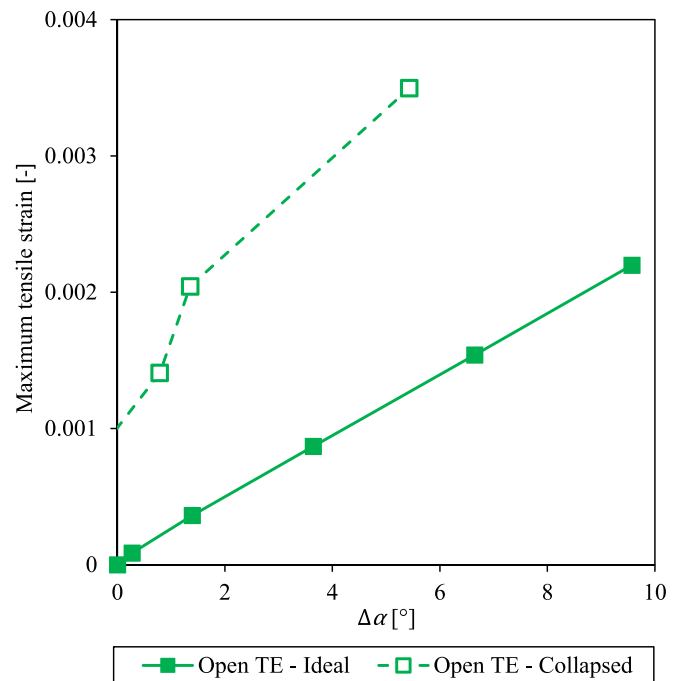rease in C_L at high water velocities with an increase in C_L at low water velocities, however, this relationship was non-linear, with diminishing returns as the angle of attack increased.

To evaluate the open TE designs in terms of load mitigation, it was useful to consider the thrust force being generated (i.e., the force normal to the chord line), as it is often the most significant loading on the blade
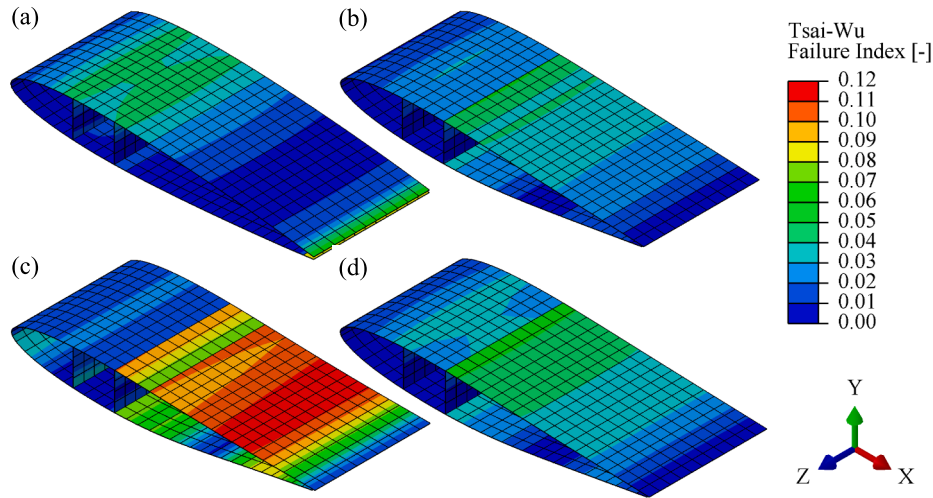
Fig. 13. Simulated Tsai-Wu failure index of the full-scale blade sections: (a) "rigid" reference blade (i.e., closed TE with a QI lay-up); (b) biaxial lay-up, $[90/0]_{2s}$; (c) triaxial lay-up, $[\pm45/0_2]_S$; (d) QI lay-up, $[90/\pm45/0]_S$.
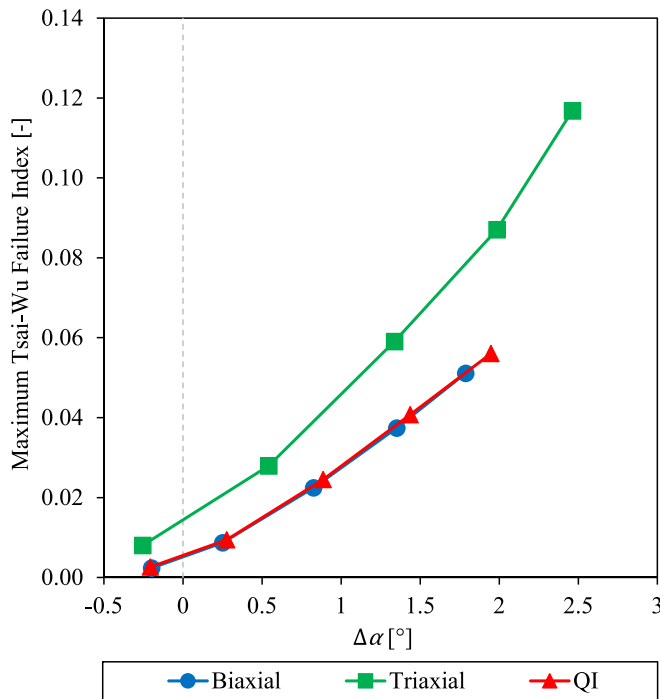

Fig. 14. The maximum Tsai-Wu failure index as a function of the change in angle of attack. Note, each set of datapoints represent equispaced time steps in a linear ramp of water velocity (1 – 5 m/s).

[17]. The thrust force, F_T [N], is calculated from the lift force, F_L [N], and drag force, F_D [N], as follows,

$$F_T = F_L\cos\alpha + F_D\sin\alpha, \tag{8}$$

$$F_L = \frac{1}{2}\rho_\infty V_R{}^2 L C_L b, \tag{9}$$

$$F_D = \frac{1}{2}\rho_\infty V_R{}^2 L C_D b, \tag{10}$$

where V_R is relative water velocity [m/s], L is the chord length [m], b is the span of the blade [m], and C_D is the drag coefficient. As can be determined from Equation (8), the lift force increases as a function of both V_R and C_L, however, C_L decreases with increasing V_R due to

morphing. In this way, the morphing blades are load-limiting. This effect is evident in Fig. 18, which shows the morphing blades compared with equivalent rigid blades. As this comparison was only for demonstration purposes, the thrust force and water velocity were normalised against hypothetical values. The rated flow velocity, V_O, was chosen on the basis that, for increased utilization, turbines are typically designed to operate slightly below the maximum expected flow velocity [8]. Assuming the original symmetric blade (i.e., NACA 0012, $\alpha_0 = 10°$) was optimised to operate at V_O, the rated thrust force, F_O, represents a load limit for the blade, which typically accounts for a safety factor of 1.35 or greater [17,27]. Under normal circumstances, a means of force regulation (e.g. active pitch control [16,47]) would be implemented for relative water velocities exceeding V_O, but, in this scenario, the rigid blades were left unregulated for a clearer comparison with the passively morphing blades.

Fig. 18 shows that the passively morphing blades achieved a significant reduction in thrust force at high water velocities (as much as 55 % reduction). It also shows that, as water velocity increased, there was a gradual divergence between the two sets of blades, rather than a sudden transition as may be seen with active pitching mechanisms [16,47]. Naturally, this was related to the linear, elastic response of the TE skins, which deformed proportionally for increasing pressure loads. Moreover, the proportionality (i.e., the slope of the curves) was a function of skin thickness. The combined tailoring of camber and skin stiffness is analogous to the concept of designing pre-bend [40], pre-load [5], or pre-twist [8] into a morphing structure, i.e., designing the structure to morph into its optimal shape for a given set of conditions. The added benefit of introducing "pre-camber", however, was that more lift was produced at lower water velocities. As the majority of a tidal turbine's operation (approx. 70 % [47]) will be spent between its cut-in speed and its rated maximum (i.e., $V_R/V_O < 1$), the use of "pre-camber" could be valuable in maximising power extraction at low-to-medium water velocities. The extent of this, however, must be balanced with the additional mechanical demand on the cambered blades (Fig. 16). Nevertheless, blade cambering offers an additional layer to the tailorability of the open TE design.

3.2.3. Potential for bend-twist coupling

The final concept tested for the full-scale open TE design was the implementation of off-axis plies to promote bend-twist coupling. As previously mentioned, this morphing mechanism has seen considerable development for HATTs that have conventional closed TE designs,
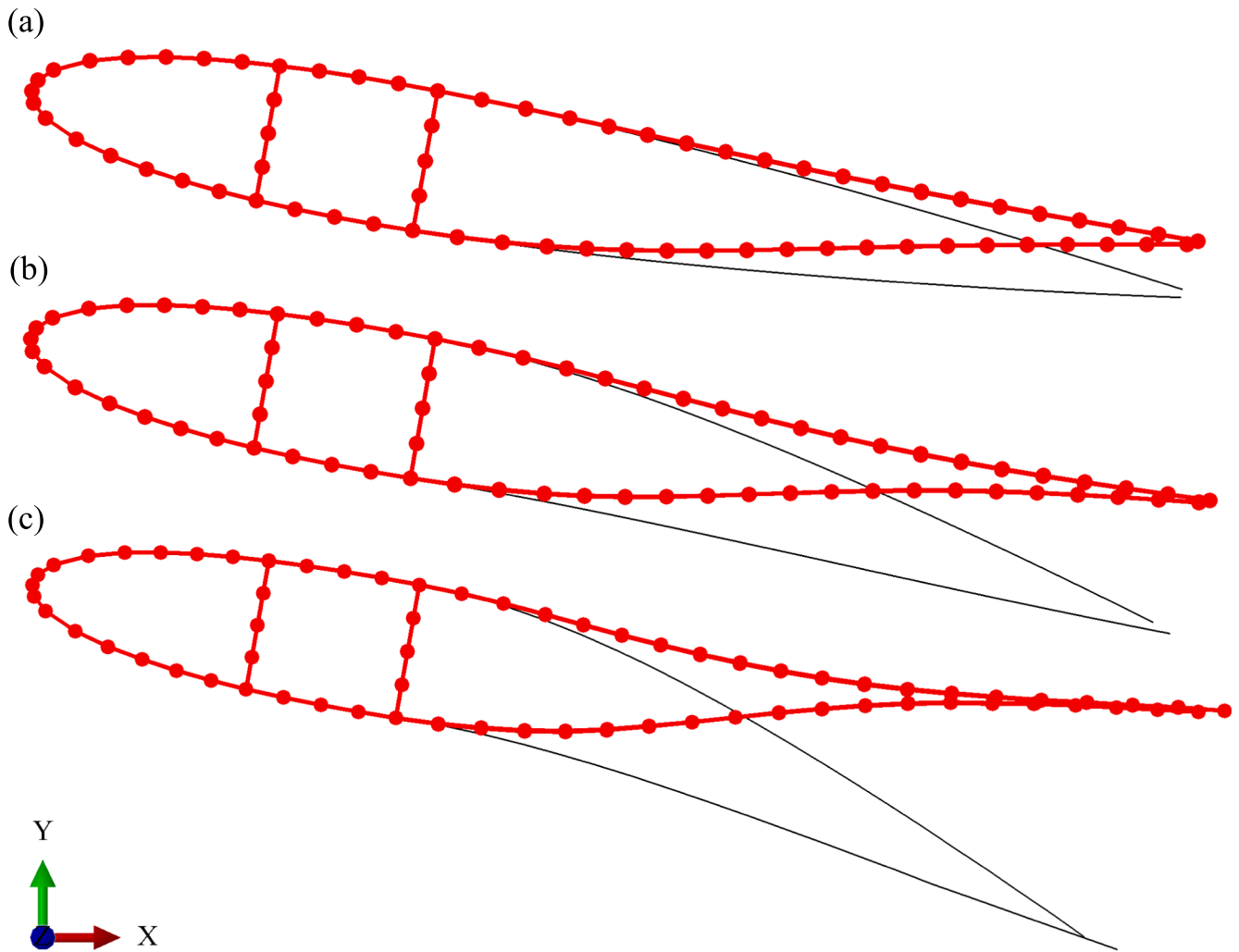
Fig. 15. FEA simulations of full-scale morphing blades with open TEs: (a) $\alpha_0 = 10°$; (b) $\alpha_0 \approx 14°$; (c) $\alpha_0 \approx 18°$. The original hydrofoil geometry is shown in black and the deformed shape at maximum water velocity (i.e., 5 m/s) is shown in red.

however, it has also been shown that open TE designs for aircraft wings provide less structural resistance to morphing via spanwise twisting [35].

Simulations were performed using a revised lay-up configuration to induce bend-twist morphing. As can be seen in Fig. 19, this resulted in spanwise (z-direction) variation of the TE displacement. The simulation was repeated for several blade configurations, the results of which are summarised in Table 4. Overall, the level of twisting was low, however, Fig. 17 shows that a 0.5°/m variation could change the local lift coefficient by up to 10 %. Moreover, over the span of a full-scale HATT blade (e.g. 8 m), a mean variation of 0.2°/m would result in a total twist of 1.6°, as in the case of [47]. It should be noted that while the presence of 0° and 90° fibres reduced the bend-twist coupling, it also reduced the likelihood of material failure. The opposite was true of introducing camber, which increased both the level of twisting and the failure index. As in the case of the QI lay-up, this was because the cambered blades had thinner skins that allowed for greater deformation.

In regard to the angle of the off-axis fibres, while others have found 30° plies to be optimal for bend-twist coupling in the flapwise direction [7,48], it was less effective for the open TE design considered herein because chordwise bending was dominant. Instead, 60° plies provided the most twist for the symmetric hydrofoil, however, 45° plies may provide a better balance for a realistic HATT blade design, due to greater contribution of flapwise bending.

3.3. Future design considerations

The present study has considered quasi-steady conditions to investigate how passively morphing TEs can be designed and manufactured using composite materials. Having identified the open TE design as a candidate for further development, the next stage would be to study its performance in unsteady hydrodynamic conditions (i.e., oscillating and fluctuating water velocity). In this regard, a significant design hurdle for the morphing structure is that the stiffness of composite materials is known to degrade as a result of fatigue cycling and water ingress [49–51]. Stiffness degradation alters the morphing response of the blade, resulting in a change to its hydrodynamic performance [47]. Naturally, this affects power generation and may also affect the stability of the blades, so it must be accounted for in the design process. One means of reducing the impact of stiffness degradation would be to combine passive morphing with active pitch control [47], such that the latter pitches to low frequency oscillations (e.g. semi-diurnal tide cycles) and the former mitigates high frequency fluctuations (e.g. wave interaction, tower shadow effects, vortex shedding, etc.). This synergistic approach would have the added benefit that, in the event of active control failure, the passive morphing mechanism could mitigate blade damage until the fault is repaired.

Another aspect of unsteady hydrodynamics to consider is the stability of the blades, both in terms of resonance and hydroelastic effects. An initial modal analysis has been performed on several of the full-scale
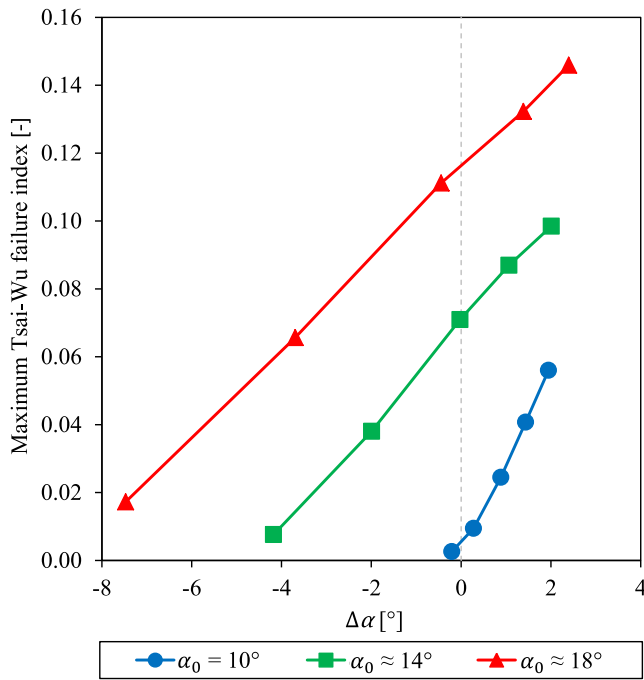
Fig. 16. Maximum Tsai-Wu failure index for the symmetric and cambered blades. Note, $\Delta\alpha$ was plotted relative to the initial angle of attack of the symmetric blades, $\alpha_0 = 10°$.
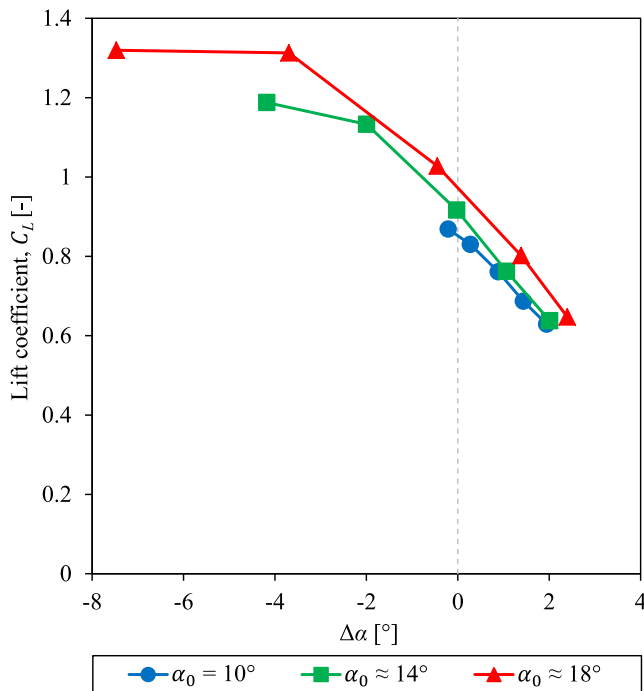

Fig. 17. Lift coefficient as a function of the change in angle of attack.

blade configurations (see Appendix B for more details), however, it was limited to predicting "in-air" resonant frequencies and mode shapes. Both the influence of water and stiffness degradation must be considered as both will contribute to lower resonant frequencies, while changes in damping can lead to hydroelastic instabilities [40,41].

Another consideration is the importance of out-of-plane stresses for the open TE design. As the skins were cantilevered, stress tended to concentrate around the transition between the box spar and trailing
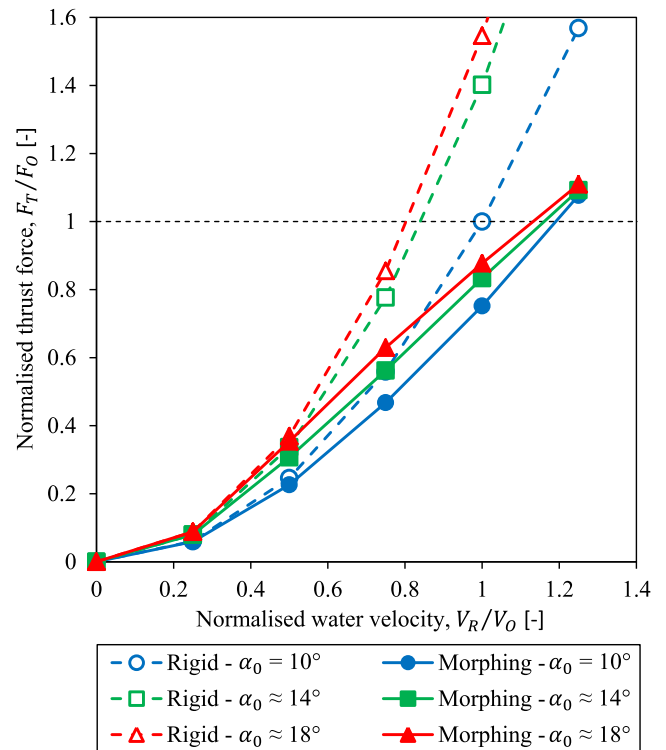

Fig. 18. Comparison of the passively morphing blades with equivalent rigid blades. Increasing the camber of the blade increased thrust at low-to-medium water velocities, while the morphing mechanism mitigated excessive thrust at high water velocities.
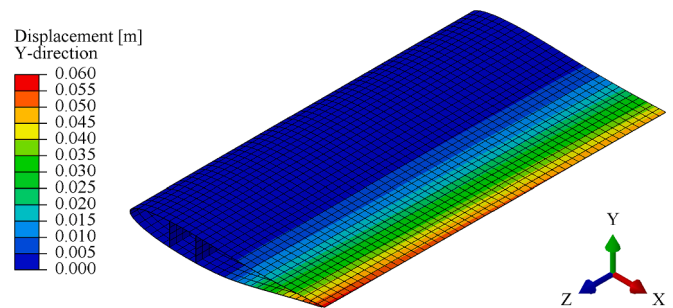

Fig. 19. FEA simulation of bend-twist coupling in a full-scale open TE blade.

Table 4
Summary of FEA results for bend-twist coupling.

Blade configuration	Twist [°/m]	Max Tsai-Wu failure index
$[90/-30_2/0]_S$, $\alpha_0 = 10°$	0.062	0.058
$[90/-45_2/0]_S$, $\alpha_0 = 10°$	0.163	0.059
$[90/-60_2/0]_S$, $\alpha_0 = 10°$	0.206	0.057
$[90/-45_2/0]_S$, $\alpha_0 = 14°$	0.536	0.102
$[90/-45_2/0]_S$, $\alpha_0 = 18°$	0.829	0.136

edge skins (shown in Fig. 13(b) and (d)). The 3D shell model, however, assumes a plane stress condition, so out-of-plane stresses are not calculated. Given that high out-of-plane stresses could result in delamination at this transition, further analysis is required to determine the 3D stress state.

Finally, further investigation is required to understand and mitigate the internal-external pressure difference that caused the flooded TE to partially collapse. Understanding the underlying mechanism will help to

determine whether TE collapse is a genuine risk at full-scale and whether it also affects HATT-type blades, which vary along the spanwise axis. In the event that mitigation is required, some methods for equalising the pressure difference could include creating holes on the high-pressure side of the blade, or incorporating hub fairing ducts to redirect water into the blades. At the same time, complete equalisation may be undesirable as the pressure difference helps to prevent TE skin separation, which usually requires a secondary linking mechanism [52,53].

4. Conclusions

This work presented the development of passively morphing trailing edge designs for composite tidal turbine blades. Three trailing edge designs were initially considered for lab-scale flume testing and simulation: a closed trailing edge, an open trailing edge, and a corrugated trailing edge. A flexible glass-fibre/epoxy system was used in all three cases. Both experiment and simulation showed that the high geometric stiffness of the closed trailing edge resulted in undesirable skin buckling. In contrast, the lower geometric stiffness of the open trailing edge and the corrugated trailing edge designs allowed them to morph easily. As such, it was concluded that lowering the material stiffness alone was insufficient to achieve morphing. Instead, it was necessary to consider both material stiffness and geometric stiffness.

Of the two successful designs, the corrugated design introduced considerably more complexity in terms of manufacturing and presented challenges in terms of bonding elastomeric skins to the composite corrugations. For this reason, the open trailing edge design was chosen for further investigation. This design presented little to no additional manufacturing complexity, as it was essentially a conventional blade design with an unbonded trailing edge. It was, however, prone to partial collapse due to internal-external pressure differences. The source and mechanism for these pressure differences are not yet fully understood and require further investigation.

Further simulations of the open trailing edge design were performed at full scale, using a glass-fibre/epoxy system with conventional mechanical properties. Initially, three lay-up configurations were investigated: biaxial $[90/0]_{2S}$, triaxial $[\pm45/0_2]_S$, and quasi-isotropic $[90/\pm45/0]_S$. For each lay-up, morphing was achieved without any collapse of the trailing edge, however, the triaxial lay-up displayed a higher failure index. It was concluded that the presence of 90° fibres was desirable to provide chordwise strength to the morphing mechanism. In the context of other typical blade loads, such as, flapwise bending, edgewise bending, and torsion, a quasi-isotropic lay-up was considered the most suitable for the open trailing edge design. As such, this lay-up was chosen to study the influence of camber.

Camber was introduced to the hydrofoil geometry such that the initial angle of attack was increased from 10° to 14° and 18°. To allow the cambered blades to morph to the same final angle of attack (8°), it

was necessary to reduce the skin thickness. This resulted in a return of the collapsing phenomenon; however, it was found that each design had a relatively low failure index. Moreover, increasing the camber of the blade helped to maintain a higher lift coefficient at low-to-medium water velocities, while morphing to a low-lift geometry at high water velocities.

Finally, the combination of chordwise morphing and bend-twist coupling was explored. It was shown that, for an appropriate lay-up, spanwise twisting could be achieved without adversely affecting the material failure index. Along with other tailorable elements of the open trailing edge design, this further highlighted its potential for use in passively morphing tidal turbine blades.

CRediT authorship contribution statement

James M. Maguire: Writing – review & editing, Writing – original draft, Visualization, Validation, Software, Project administration, Methodology, Investigation, Formal analysis, Conceptualization. **Dimitrios Mamalis:** Writing – review & editing, Validation, Project administration, Methodology, Investigation, Conceptualization. **Shūji Ōtomo:** Writing – review & editing, Validation, Resources, Investigation. **Edward D. McCarthy:** Writing – review & editing, Supervision, Resources, Project administration, Methodology, Funding acquisition, Conceptualization.

Declaration of competing interest

The authors declare that they have no known competing financial interests or personal relationships that could have appeared to influence the work reported in this paper.

Data availability

Data will be made available on request.

Acknowledgements

Appendix A – Design of trailing edge concepts

A.1. Comparison of open and closed the trailing edges

The cross-section of a closed TE can be approximated as a hollow triangular section; a geometry which is inherently stiff. As such, the skins of the hydrofoil must be highly compliant to allow it to morph. Such a system is proposed by Cognet et al. [54] for morphing wind turbine blades, however, achieving the necessary compliance, while ensuring the skins can survive 20 + years of operation, is not trivial. The pure polymer skins suggested in [54] are unlikely to be suitable mechanically, while conventional composite skins are much too stiff, leading to undesirable deformations like skin buckling [52].

An alternative is to open the TE tip, so that the upper and lower skins are free to bend independently of each other. A similar approach has been investigated for morphing aircraft wings with an internal active pitching mechanism for in-flight control, which allows the skins to slide past each other to avoid skin buckling [35,52,53]. For the current study, the open TE design is applied as a passive mechanism to avoid the added expense and/or complexity associated with active pitching mechanisms. To elaborate on this concept, it is worthwhile to compare the second moment of area of an open TE with that of a closed TE. In the case of an open TE, the upper and lower skins are approximated as single, independent cantilever plates with rectangular cross-sections. Assuming a constant skin thickness t [m], the second moment of area, I_O [m^4], for this case is,

$$I_O = \frac{bt^3}{12},$$
(A.1)

where b is the span of the blade [m].

In the case of a closed TE, determining the second moment of area is more complex as the skins converge together over the chord length. As a simplification, the skins are approximated as two converging rectangular cross-sections equidistant from the neutral axis along the chord. Using the parallel axis theorem, the second moment of area, I_C [m^4], at a given point, x, along the chord line is,

$$I_C(x) = 2\left(I_O + A_C d(x)^2\right) = \frac{2bt^3}{12} + 2btd(x)^2,$$
(A.2)

where A_C is the area of the cross-section [m^2] and d is the distance from the neutral axis to the centre of mass of the section [m], which is approximately half of the hydrofoil thickness at a given point, x.

Combining Eqs. (A.1) and (A.2), the ratio of the second moment of area at a given point, x, along the chord line can be expressed as,

$$\frac{I_C(x)}{I_O} = 2 + \frac{24d(x)^2}{t^2}.$$
(A.3)

Using Equation (A.3), the influence of hydrofoil thickness and skin thickness is displayed over a broad range in Fig. A.1. Assuming the hydrofoil thickness is controlled by hydrodynamic design, the skin thickness is the dominant design factor for controlling the second moment of area of the TE.

Of course, the second moment of area must be evaluated over the entire length of the TE, l [m]. Integrating Equation (A.2), with respect to x gives an equivalent second moment of area for the closed TE,

$$I_C = \frac{1}{l} \int_0^l I_C(x)dx.$$
(A.4)

Applying Eqs. (A.1) and (A.4) to a lab-scale NACA 0012 hydrofoil with a profile thickness of 18 mm and 0.5 mm skin thickness, opening the TE can reduce its chordwise second moment of area by a factor of 3100; note, cumulative integration was performed in Matlab and verified in Abaqus FEA. An analogous approach was taken by Vos et al. [35] when comparing open and closed TEs in torsion. They analysed a NACA 23012 airfoil and found that opening the TE skins could reduce the second polar moment of area by a factor of almost 10^4, however, they noted that this came at the compromise of load-carrying capacity. Likewise, opening the TE of a conventional blade would likely lead to progressive damage and failure of the blade [38] if the reduced stiffness was not taken into account. For this reason, any blade with an open TE would require additional compensatory reinforcement of the box spar and LE. Nevertheless, relating I_C/I_O back to Equation (1), where the deflection is inversely proportional to the second moment of area, highlights the potential of this morphing concept.
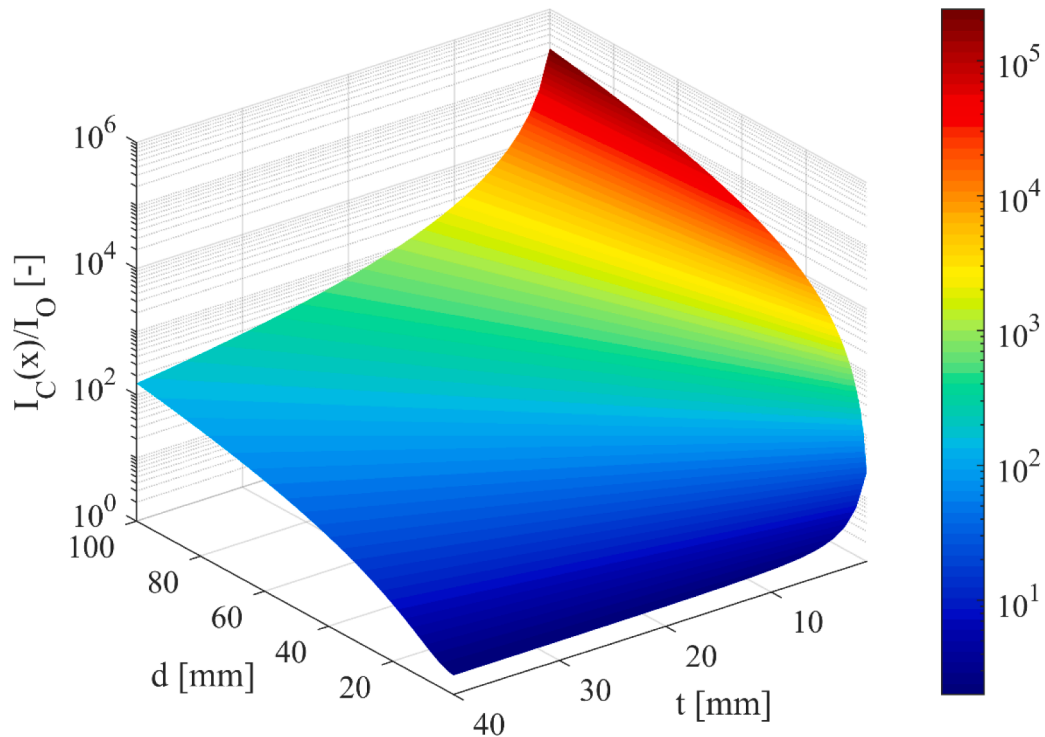

Fig. A1. Contour map of $I_C(x)/I_O$ for varying skin thickness, t, and hydrofoil half-thickness, d.

A.2. Corrugated composite skin design

Through another manipulation of geometry, corrugated laminates allow for the introduction of anisotropic axial and bending stiffnesses. Combined with anisotropic composite lay-ups, it is possible to exert a high degree of control over the directional compliance of the structure. For composite laminates, the axial stiffness, $\overline{A}_{11}$ [N/m], and bending stiffness, $\overline{D}_{11}$ [N m], of trapezoidal corrugation (see the illustration in Table A.1) in the morphing direction can be described by the following equations from [55],

$$\overline{A}_{11} = \frac{2c}{\frac{I_1}{A_{11}} + \frac{I_2}{D_{11}}}, \tag{A.5}$$

$$\overline{D}_{11} = \frac{c}{s}D_{11}, \tag{A.6}$$

where c is the length of the corrugated semi-period [m] and s is the length of the corrugated profile [m], which can be expressed as,

$$c = \frac{2h}{\tan\theta} + r, \tag{A.7}$$

$$s = \frac{2h}{\sin\theta} + r, \tag{A.8}$$

where h is the height of the semi-period [m], θ is the angle of the corrugation [rad], and r is the base length on the corrugation [m].

I_1 and I_2 in Equation (A.5) are geometric parameters [m] that can be calculated as follows,

$$I_1 = \frac{4(h/2)\cos\theta}{3\sin\theta} + 2c - \frac{4(h/2)}{\tan\theta}, \tag{A.9}$$

$$I_2 = \frac{4(h/2)^3}{3\sin\theta} + 2(h/2)^2\left(c - \frac{h}{\tan\theta}\right). \tag{A.10}$$

A_{11} and D_{11} in Equation (A.5) are the axial stiffness [N/m] and bending stiffness [N m], respectively, of an equivalent flat laminate (i.e., without corrugation),

$$A_{11} = E_{11}t, \tag{A.11}$$

$$D_{11} = \frac{E_{11}t^3}{12}, \tag{A.12}$$

where E_{11} is the Young's modulus in the morphing direction and t is the thickness of the laminate.

Thus, there are four geometric parameters that need to be defined; t, h, θ, and r. Using Eqs. (A.5) –(A.12), a parametric study was performed to determine the sensitivity of the axial and bending stiffnesses (in the morphing direction) to the geometric parameters of the corrugation; note, the accuracy of these equations was verified by simulations in Abaqus FEA. Each parameter was varied over a range while the remaining parameters were kept constant e.g. t was varied between 1 mm and 9 mm while r, h, and θ were kept constant at 15 mm, 9 mm, and 50°, respectively. Table A.1 gives further details of the values used in the parametric study.

Table A1
Input values for the parametric study of a laminate with trapezoidal corrugations.

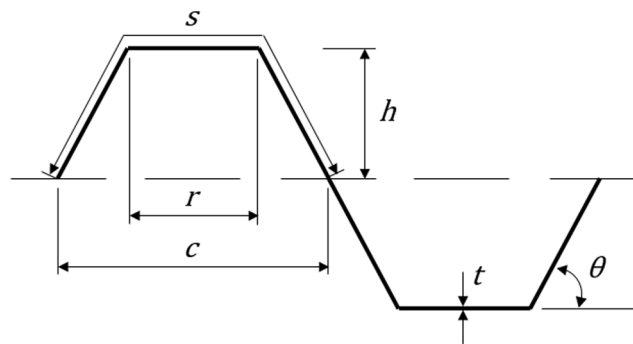| Parameter [units]	Range	Constant value
Thickness, t [m]	0.001 – 0.009	0.005
Base length, r [m]	0.005 – 0.025	0.015
Semi-period height, h [m]	0.003 – 0.015	0.009
Corrugation angle, θ [°]	10 – 90	50

Figure A.2 shows the results of the parametric study. To compare the results for different parameters, the axial and bending stiffnesses (Eqs. (A.5)

and (A.6), respectively) were normalised against values for an equivalent flat composite laminate (Eqs. (A.11) and (A.12), respectively). In general, the axial stiffness was reduced more by the corrugation than bending stiffness, and had a higher sensitivity to variation in thickness, t, and semi-period height, h (see Fig. A.2(a) and (c), respectively). In comparison, the bending stiffness was unaffected by thickness, t, and was most sensitive to the angle of the corrugation, θ (see Fig. A.2(d)).
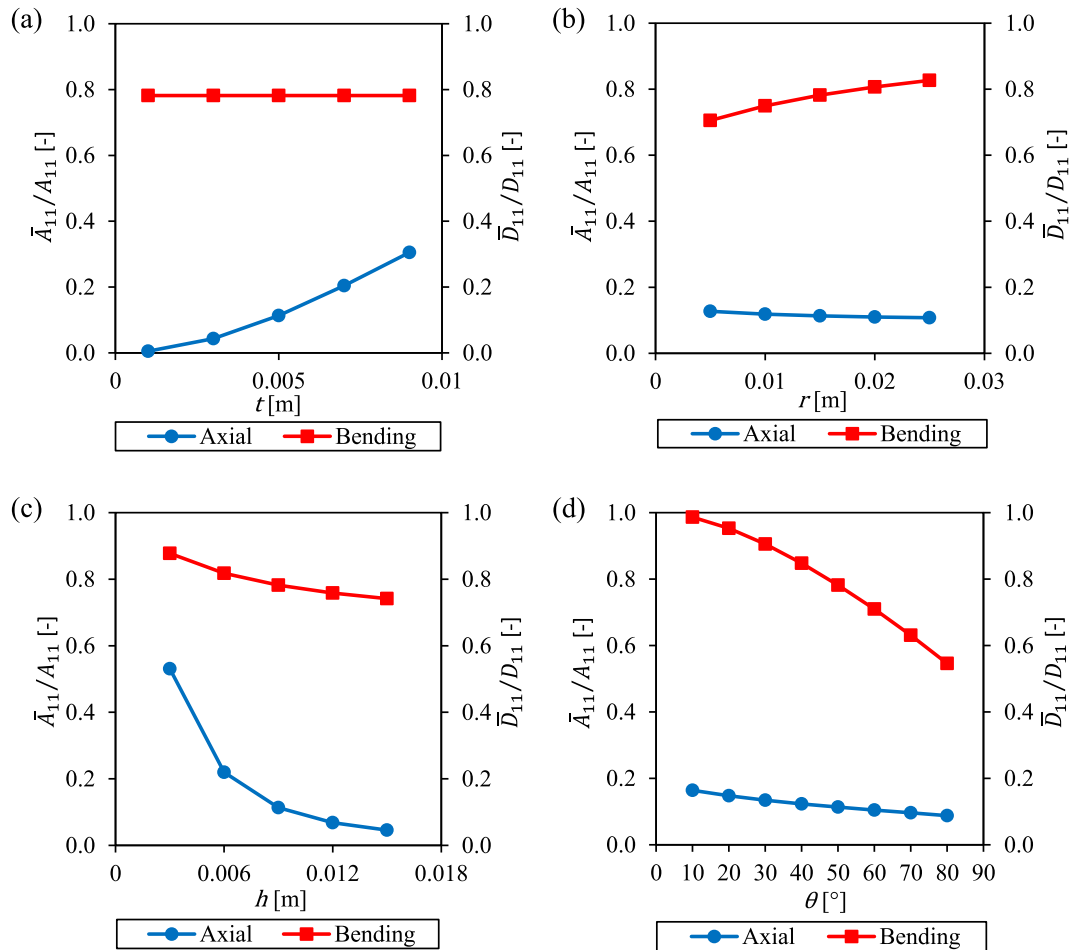

Fig. A2. Parametric study of trapezoidal corrugation in the morphing direction. The normalised axial stiffness and bending stiffness are shown on the left and right y-axes, respectively. For each plot, one geometric parameter was varied while the others remained constant; refer to Table A.1 for further details.

Appendix B: Modal analysis

While a full hydroelastic analysis of the open TE blades was outside the scope of this work, it was important to consider the stability of passively morphing TE design for future development. As a first approach, a modal analysis of blades was performed in Abaqus FEA to determine their "in-air" natural frequencies (i.e., resonant frequencies) and their mode shapes. Frequencies and mode shapes were extracted using a linear perturbation procedure. The natural frequencies for the first six modes are shown in Table B.1, with an example of the mode shapes for one blade shown in Fig. B.1. As can be seen from Table B.1, the natural frequencies varied considerable depending on the stiffness of the blade configuration. Overall, the largest change resulted from opening the TE. For the open TE designs, stiffness variation arose from differences in fibre orientation and skin thickness. For example, the mode 1 and 2 frequencies of the biaxial and QI lay-ups were higher than the triaxial lay-up because the mode shapes were chordwise bending (see Fig. B.1(a) and (b)), but the reverse was true for the mode 5 and 6 frequencies because they were torsional modes (see Fig. B.1(e) and (f)).
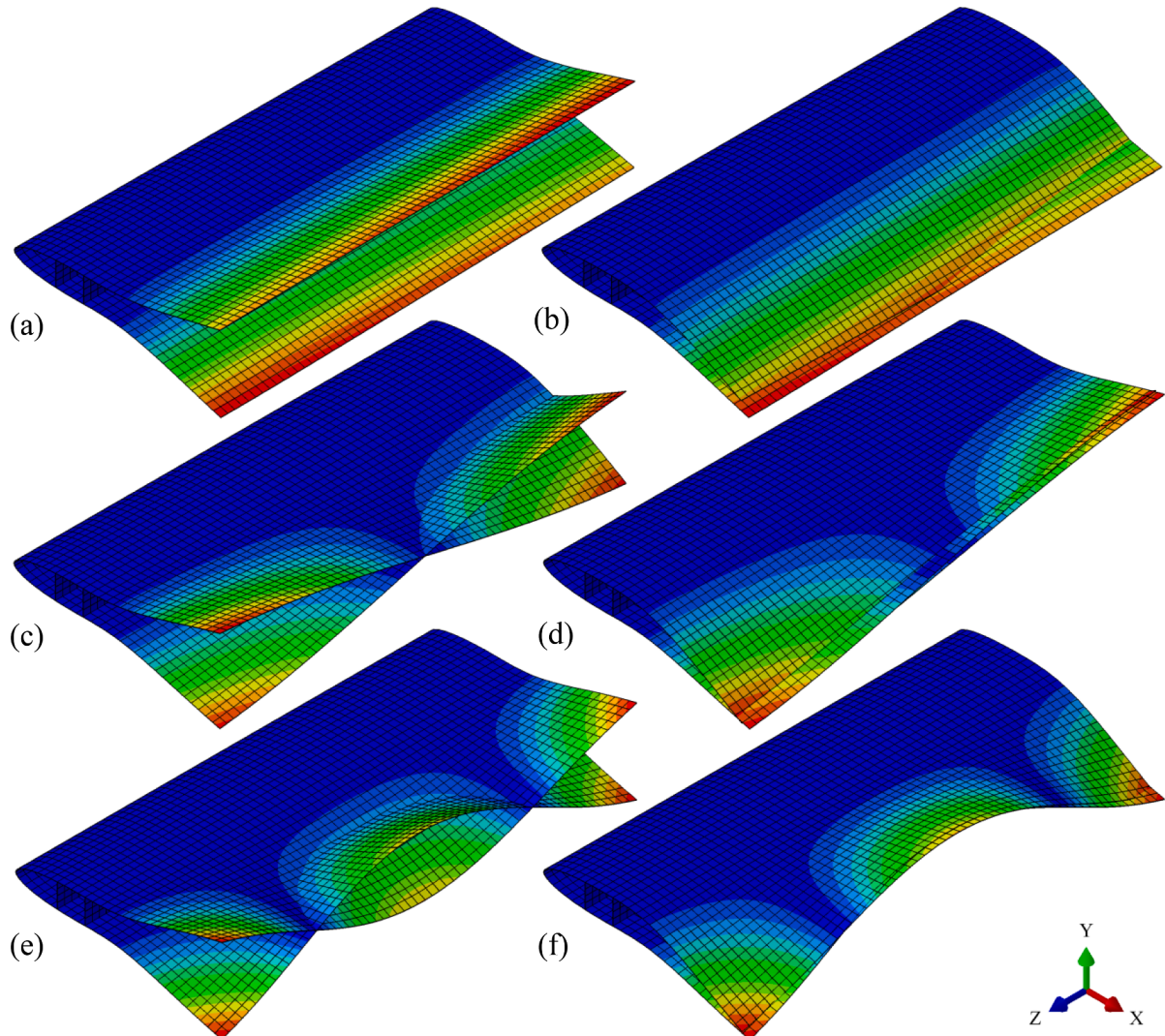
Table B1
Resonant frequencies of the various full-scale blade configurations. All but the first blade configuration are open TE designs.

Blade configuration	Frequency [Hz]					
	Mode 1	Mode 2	Mode 3	Mode 4	Mode 5	Mode 6
QI, rigid (i.e., closed TE)	43.6	57.7	74.1	98.0	102	104
Biaxial, $\alpha_0 = 10°$	11.2	11.2	12.0	12.0	17.0	17.5
Triaxial, $\alpha_0 = 10°$	7.69	7.71	10.2	10.3	18.9	19.5
QI, $\alpha_0 = 10°$	10.4	10.4	11.8	11.8	18.0	18.7
QI, $\alpha_0 \approx 14°$	7.39	7.42	8.37	8.49	11.4	16.8
QI, $\alpha_0 \approx 18°$	6.09	6.14	6.97	7.06	11.6	16.4

In each case, the natural frequencies were above what would be expected for high amplitude loading of a blade (e.g. < 2 Hz for rotational loading and wave loading [9,10,56,57]), however, it must be considered that these are "in-air" natural frequencies. Kramer et al. [58] have shown that the "in-

water" natural frequencies can be 50 – 70 % lower than "in-air" natural frequencies. Although water will dampen the dynamic behavior of the blade [5], a similar reduction in natural frequency for the hydrofoil could put the structure at risk of resonant vibration. Modelling the "in-water" natural frequency in Abaqus FEA is non-trivial [48], particularly in the case of a hydrofoil geometry, however it should be considered for future investigations. Future studies should also consider a holistic approach to hydroelastic design, similar to that of aeroelastic design for wind turbines [40], i.e., analyses should include other turbine components and the interactions between them.

Fig. B1. Mode shapes for a full-scale blade (QI, $\alpha_0 = 10°$): (a – f) Mode 1–6 (see also Table B.1). Note, the contour colour map is excluded as the displacement magnitudes are not true physical quantities.

Appendix C. Supplementary data

Supplementary data to this article can be found online at https://doi.org/10.1016/j.compstruct.2024.118090.

References

[1] Segura E, Morales R, Somolinos JA, López A. Techno-economic challenges of tidal energy conversion systems: current status and trends. Renew Sustain Energy Rev 2017;77:536–50. https://doi.org/10.1016/j.rser.2017.04.054.

[2] Waldman S. Here's why UK tides are soon going to play a much bigger part in powering your home. accessed December 8, 2022 Conversat 2022. https://theconversation.com/heres-why-uk-tides-are-soon-going-to-play-a-much-bigger-part-in-powering-your-home-176719.

[3] Walker S, Thies PR. A review of component and system reliability in tidal turbine deployments. Renew Sustain Energy Rev 2021;151:111495. https://doi.org/10.1016/j.rser.2021.111495.

[4] Kennedy CR, Leen SB, Brádaigh CMÓ. A preliminary design methodology for fatigue life prediction of polymer composites for tidal turbine blades. Proc Inst Mech Eng Part L J Mater Des Appl 2012;226:203–18. https://doi.org/10.1177/1464420712443330.

[5] Pisetta G, Le Mestre R, Viola IM. Morphing blades for tidal turbines: a theoretical study. Renew Energy 2022;183:802–19. https://doi.org/10.1016/j.renene.2021.10.085.

[6] Nicholls-Lee RF, Turnock SR, Boyd SW. Application of bend-twist coupled blades for horizontal axis tidal turbines. Renew Energy 2013;50:541–50. https://doi.org/10.1016/j.renene.2012.06.043.

[7] Murray RE, Doman DA, Pegg MJ. Finite element modeling and effects of material uncertainties in a composite laminate with bend-twist coupling. Compos Struct 2015;121:362–76. https://doi.org/10.1016/j.compstruct.2014.11.035.

[8] Murray RE, Nevalainen T, Gracie-Orr K, Doman DA, Pegg MJ, Johnstone CM. Passively adaptive tidal turbine blades: design tool development and initial verification. Int J Mar Energy 2016;14:101–24. https://doi.org/10.1016/j.ijome.2016.02.001.

[9] Murray RE, Ordonez-Sanchez S, Porter KE, Doman DA, Pegg MJ, Johnstone CM. Towing tank testing of passively adaptive composite tidal turbine blades and comparison to design tool. Renew Energy 2018;116:202–14. https://doi.org/10.1016/j.renene.2017.09.062.

[10] Porter KE, Ordonez-Sanchez SE, Murray RE, Allmark M, Johnstone CM, O'Doherty T, et al. Flume testing of passively adaptive composite tidal turbine blades under combined wave and current loading. J Fluids Struct 2020;93:102825. https://doi.org/10.1016/j.jfluidstructs.2019.102825.

[11] Hoerner S, Kösters I, Vignal L, Cleynen O, Abbaszadeh S, Maître T, et al. Cross-flow tidal turbines with highly flexible blades—Experimental flow field investigations at strong fluid–structure interactions. Energies 2021:14. https://doi.org/10.3390/en14040797.

[12] Tully S, Viola IM. Reducing the wave induced loading of tidal turbine blades through the use of a flexible blade. 16th Int. Symp. Transp. Phenom. Dyn. Rotating Mach. ISROMAC, Honolulu, USA: 2016.

[13] Zeiner-Gundersen DH. A novel flexible foil vertical axis turbine for river, ocean, and tidal applications. Appl Energy 2015;151:60–6. https://doi.org/10.1016/j.apenergy.2015.04.005.

[14] Descoteaux PO, Olivier M. Performances of vertical-axis hydrokinetic turbines with chordwise-flexible blades. J Fluids Struct 2021;102:103235. https://doi.org/10.1016/j.jfluidstructs.2021.103235.

[15] Arredondo-Galeana A, Kiprakis A, Viola IM. A low cost oscillating membrane for underwater applications at low Reynolds numbers. J Mar Sci Eng 2022:10. https://doi.org/10.3390/jmse10010077.

[16] Fagan EM, Kennedy CR, Leen SB, Goggins J. Damage mechanics based design methodology for tidal current turbine composite blades. Renew Energy 2016;97:358–72. https://doi.org/10.1016/j.RENENE.2016.05.093.

[17] Grogan DM, Leen SB, Kennedy CR, Brádaigh CMÓ. Design of composite tidal turbine blades. renew. Energy 2013;57:151–62. https://doi.org/10.1016/J.RENENE.2013.01.021.

[18] Delafin PL, Deniset F, Astolfi JA, Hauville F. Performance improvement of a darrieus tidal turbine with active variable pitch. Energies 2021;14:1–18. https://doi.org/10.3390/en14030667.

[19] Mannion B, McCormack V, Kennedy C, Leen SB, Nash S. An experimental study of a flow-accelerating hydrokinetic device. Proc Inst Mech Eng Part A J Power Energy 2019;233:148–62. https://doi.org/10.1177/0957650918772626.

[20] Han SH, Park JS, Lee KS, Park WS, Yi JH. Evaluation of vertical axis turbine characteristics for tidal current power plant based on in situ experiment. Ocean Eng 2013;65:83–9. https://doi.org/10.1016/j.oceaneng.2013.03.005.

[21] Budynas RG, Nisbett JK, Shigley JE. Shigley's mechanical engineering design. McGraw-Hill; 2011.

[22] Li D, Zhao S, Da Ronch A, Xiang J, Drofelnik J, Li Y, et al. A review of modelling and analysis of morphing wings. Prog Aerosp Sci 2018;100:46–62. https://doi.org/10.1016/j.paerosci.2018.06.002.

[23] Easy Composites Ltd. EF80 Flexible Epoxy Resin - Technical Data Sheet. 2020.

[24] Floreani C, Cuthill F, Steynor J, Maguire JM, McCarthy ED, Niessink MJ, et al. Testing of a 6 m hybrid Glass/Carbon fibre powder epoxy composite wind blade demonstrator. SAMPE J 2021. May/June:6–14.

[25] Finnegan W, Allen R, Glennon C, Maguire J, Flanagan M, Flanagan T. Manufacture of high-performance tidal turbine blades using advanced composite Manufacturing technologies. Appl Compos Mater 2021. https://doi.org/10.1007/s10443-021-09967-y.

[26] Maguire JM, Sharp ND, Pipes RB, Brádaigh CMÓ. Advanced process simulations for thick-section epoxy powder composite structures. Compos Part A Appl Sci Manuf 2022:161. https://doi.org/10.1016/j.compositesa.2022.107073.

[27] Jiang Y, Finnegan W, Wallace F, Flanagan M, Flanagan T, Goggins J. Structural analysis of a fibre-reinforced composite blade for a 1 MW tidal turbine rotor under degradation of seawater. J Ocean Eng Mar Energy 2023. https://doi.org/10.1007/s40722-023-00279-w.

[28] ASTM D3039/D3039M. Standard Test Method for Tensile Properties of Polymer Matrix Composite Materials. 2014. 10.1520/D3039.

[29] ASTM D 3518. Standard Test Method for In-Plane Shear Response of Polymer Matrix Composite Materials by Tensile Test of a ±45 ° Laminate. 2018. 10.1520/D3518.

[30] Drela M. XFOIL: an analysis and design system for low Reynolds number airfoils. In: Mueller TJ, editor. Low Reynolds Number Aerodyn., Heidelberg, Germany: Springer-Verlag Berlin; 1989, p. 1–12. 10.1007/978-3-642-84010-4_1.

[31] Leishman JG. Principles of helicopter aerodynamics. Cambridge University Press; 2006.

[32] Whelan JI, Graham JMR, Peiró J. A free-surface and blockage correction for tidal turbines. J Fluid Mech 2009;624:281–91. https://doi.org/10.1017/S0022112009005916.

[33] Gambuzza S, Ōtomo S, Liu Y, Young A, Broglia R, McCarthy E, et al. Design and Demonstration of a Passive Pitch System for Tidal Turbines. Proc. 15th Eur. Wave Tidal Energy Conf., vol. 15, Bilbao, Spain: 2023. 10.36688/ewtec-2023-504.

[34] Clancy LJ. Aerodynamics. London: Pitman Publishing Limited; 1973.

[35] Vos R, Gürdal Z, Abdalla M. Mechanism for warp-controlled twist of a morphing wing. J Aircr 2010;47:450–7. https://doi.org/10.2514/1.39328.

[36] Hu N, Burgueño R. Buckling-induced smart applications: recent advances and trends. Smart Mater Struct 2015;24. https://doi.org/10.1088/0964-1726/24/6/063001.

[37] Molholt Jensen F, Branner K. 1 - introduction to wind turbine blade design. Adv Wind Turbine Bl Des Mater, Woodhead Publishing Limited 2013:3–28. https://doi.org/10.1533/9780857097286.1.3.

[38] Chen X, Berring P, Madsen SH, Branner K, Semenov S. Understanding progressive failure mechanisms of a wind turbine blade trailing edge section through subcomponent tests and nonlinear FE analysis. Compos Struct 2019;214:422–38. https://doi.org/10.1016/J.COMPSTRUCT.2019.02.024.

[39] Lahuerta F, Koorn N, Smissaert D. Wind turbine blade trailing edge failure assessment with sub-component test on static and fatigue load conditions. Compos Struct 2018;204:755–66. https://doi.org/10.1016/J.COMPSTRUCT.2018.07.112.

[40] Holierhoek JG. Chapter 5 - aeroelastic design of wind turbine blades. advances in wind turbine blade design and materials. Woodhead Publishing Limited 2013. https://doi.org/10.1533/9780857097286.1.150.

[41] Li D, Guo S, Xiang J. Modeling and nonlinear aeroelastic analysis of a wing with morphing trailing edge. Proc Inst Mech Eng Part G J Aerosp Eng 2012;227:619–31. https://doi.org/10.1177/0954410012438341.

[42] Yokozeki T, Sugiura A, Hirano Y. Development and Wind Tunnel Test of Variable Camber Morphing Wing. 22nd AIAA/ASME/AHS Adapt. Struct. Conf., Maryland, USA: 2014.

[43] Dayyani I, Shaw AD, Saavedra Flores EI, Friswell MI. The mechanics of composite corrugated structures: a review with applications in morphing aircraft. Compos Struct 2015;133:358–80. https://doi.org/10.1016/j.compstruct.2015.07.099.

[44] Carlsson LA, Adams DF, Pipes RB. Experimental Characterization of advanced composite materials. 4th ed. CRC Press; 2014.

[45] Jones RM. Mechanics of composite materials. 2nd ed. New York, USA: Taylor & Francis; 1999.

[46] Tsai SW, Hahn HT. Introduction to composite materials. Lancaster, PA: Technomic; 1980.

[47] Motley MR, Barber RB. Passive control of marine hydrokinetic turbine blades. Compos Struct 2014;110:133–9. https://doi.org/10.1016/j.compstruct.2013.11.026.

[48] Liao Y, Garg N, Martins JRRA, Young YL. Viscous fluid – structure interaction response of composite hydrofoils. Compos Struct 2019;212:571–85. https://doi.org/10.1016/j.compstruct.2019.01.043.

[49] Carlsson LA, Du E. Water Uptake in Polymer Composites with Voids. In: Davies P, Rajapakse YDS, editors. Durab. Compos. a Mar. Environ. 2, Springer; 2018, p. 33–58. 10.1007/978-3-319-65145-3_13.

[50] Mamalis D, Floreani C, Brádaigh CMÓ. Influence of hygrothermal ageing on the mechanical properties of unidirectional carbon fibre reinforced powder epoxy composites. Compos Part B Eng 2021;225. https://doi.org/10.1016/j.compositesb.2021.109281.

[51] Alam P, Mamalis D, Robert C, Floreani C, Brádaigh CMÓ. The fatigue of carbon fibre reinforced plastics - a review. Compos Part B Eng 2019;166:555–79. https://doi.org/10.1016/j.compositesb.2019.02.016.

[52] Di Matteo N, Guo S, Ahmed S, Li D. Design and analysis of a morphing flap structure for high lift wing. 51st AIAA/ASME/ASCE/AHS/ASC Struct. Struct. Dyn. Mater. Conf., Orlando, FL, USA: 2010, p. 1–12. 10.2514/6.2010-3096.

[53] Monner HP. Realization of an optimized wing camber by using formvariable flap structures. Aerosp Sci Technol 2001;5:445–55. https://doi.org/10.1016/S1270-9638(01)01118-X.

[54] Cognet V, Courrech du Pont S, Thiria B. Material optimization of flexible blades for wind turbines. renew. Energy 2020;160:1373–84. https://doi.org/10.1016/j.renene.2020.05.188.

[55] Airoldi A, Sala G, Di Landro LA, Bettini P, Gilardelli A. Chapter 9 - Composite Corrugated Laminates for Morphing Applications. Morphing Wing Technologies. Elsevier Ltd; 2018. 10.1016/B978-0-08-100964-2.00009-5.

[56] Lam R, Lopez Dubon S, Sellar B, Vogel C, Davey T, Steynor J. Temporal and spatial characterisation of tidal blade load variation for structural fatigue testing. Renew Energy 2023;208:665–78. https://doi.org/10.1016/j.renene.2023.03.117.

[57] Finnegan W, Fagan E, Flanagan T, Doyle A, Goggins J. Operational fatigue loading on tidal turbine blades using computational fluid dynamics. Renew Energy 2020;152:430–40. https://doi.org/10.1016/J.RENENE.2019.12.154.

[58] Kramer MR, Liu Z, Young YL. Free vibration of cantilevered composite plates in air and in water. Compos Struct 2013;95:254–63. https://doi.org/10.1016/j.compstruct.2012.07.017.